Multiscale model calibration by inverse analysis for nonlinear simulation of masonry structures under earthquake loading

Corrado Chisari[1], Lorenzo Macorini[2], Bassam A. Izzuddin[3]

Abstract

The prediction of the structural response of masonry structures under extreme loading conditions, including earthquakes, requires the use of advanced material descriptions to represent the nonlinear behaviour of masonry. In general, micro- and mesoscale approaches are very computationally demanding, thus at present they are used mainly for detailed analysis of small masonry components. Conversely macroscale models, where masonry is assumed as a homogeneous material, are more efficient and suitable for nonlinear analysis of realistic masonry structures. However, the calibration of the material parameters for such models, which is generally based on physical testing of entire masonry components, remains an open issue. In this paper, a multiscale approach is proposed, in which an accurate mesoscale model accounting for the specific masonry bond is utilised in virtual tests for the calibration of a more efficient macroscale representation assuming energy equivalence between the two scales. Since the calibration is performed offline at the beginning of the analysis, the method is computationally attractive compared to alternative homogenisation techniques. The proposed methodology is applied to a case study considering the results obtained in previous experimental tests on masonry components subjected to cyclic loading, and on a masonry building under pseudo-dynamic conditions representing earthquake loading. The results confirm the potential of the proposed approach and highlight some critical issues, such as the importance of selecting

[1] Department of Civil and Environmental Engineering, Imperial College London, South Kensington Campus, London SW7 2AZ, United Kingdom. Email: c.chisari12@imperial.ac.uk

[2] Department of Civil and Environmental Engineering, Imperial College London, South Kensington Campus, London SW7 2AZ, United Kingdom. Email: l.macorini@imperial.ac.uk

[3] Department of Civil and Environmental Engineering, Imperial College London, South Kensington Campus, London SW7 2AZ, United Kingdom. Email: b.izzuddin@imperial.ac.uk

appropriate virtual tests for model calibration, which can significantly influence accuracy and robustness.

Keywords: Multi-objective optimisation, macroscale modelling, mesoscale modelling, virtual test, dynamic analysis, plastic-damage model.

List of symbols

General

$\boldsymbol{\sigma}^{\boldsymbol{M}}$, $\boldsymbol{\sigma}^{\boldsymbol{m}}$: stress (*M*: macroscale; *m*: mesoscale)

$\boldsymbol{\varepsilon}^{\boldsymbol{M}}$, $\boldsymbol{\varepsilon}^{\boldsymbol{m}}$: strain (*M*: macroscale; *m*: mesoscale)

$\boldsymbol{\kappa}^{\boldsymbol{M}}$, $\boldsymbol{\kappa}^{\boldsymbol{m}}$: historical variables (*M*: macroscale; *m*: mesoscale)

$\epsilon(t)$: cumulative error between macroscale representation and mesoscale representation at time t

$\boldsymbol{p}$: material parameters

$\omega_1 = \epsilon(T)$: discrepancy function 1

ω_2 : discrepancy function 2

$\boldsymbol{\Phi}^{\boldsymbol{M}}$, $\boldsymbol{\Phi}^{\boldsymbol{m}}$: feature vector (*M*: macroscale; *m*: mesoscale)

$\bar{\boldsymbol{\sigma}}$: effective stress

$\boldsymbol{\varepsilon}_{\boldsymbol{e}}$: elastic strain

$\boldsymbol{\varepsilon}^{\boldsymbol{p}}$: plastic strain

$\hat{\boldsymbol{\varepsilon}}^{\boldsymbol{p}}$: plastic strain direction

Mesoscale model

c : cohesion

φ : friction angle

f_t : tensile strength

Macroscale model

κ_t, κ_c : historical variables in tension and compression

$f_t(\kappa_t), f_c(\kappa_c)$: strength in tension and compression (nominal stress space)

$\bar{f}_t(\kappa_t), \bar{f}_c(\kappa_c)$: strength in tension and compression (effective stress space)

$d_t(\kappa_t), d_c(\kappa_c)$: damage in tension and compression

F : yielding function

g : plastic flow potential

$\boldsymbol{h}$: hardening rule

ϵ : flow potential eccentricity

I_1: first invariant of stress tensor

J_2 : second invariant of deviatoric stress tensor

ψ : dilatancy angle

f_{b0r}: ratio between biaxial and uniaxial compressive strength

K_c: ratio of the second stress invariant on the tensile meridian to that on the compressive meridian at initial yield

w_t, w_c parameters governing stiffness recovery respectively from compression to tension and viceversa

$p_{1\chi}, p_{2\chi}, p_{3\chi}, p_{4\chi}$ parameters for strength functions ($\chi = t, c$)

$f_{\chi 0}$: initial strength ($\chi = t, c$)

$f_{\chi,max}$: maximum strength ($\chi = t, c$)

G_t : fracture energy (in tension)

μ : ratio between residual plastic strain and total strain when plastic work reaches s times fracture energy (in tension)

ρ : ratio of plastic strain at maximum strength when damage starts (in compression)

1 Introduction

Numerical modelling of masonry structures is currently an active and challenging research field in structural engineering. The mechanical behaviour of unreinforced masonry (URM) buildings and monuments, especially under extreme loading conditions is very complex and can be accurately predicted only when allowing for masonry material nonlinearity. This is due not only to the independent behaviour of the masonry constituents, e.g. mortar joints and units, but it is also related to the specific masonry bond. Recently, several numerical strategies for nonlinear analysis of URM structures have been developed. These include micro- or mesoscale models, where the individual masonry constituents are modelled separately (Lotfi & Shing, 1994; Lourenço & Rots, 1997; Gambarotta & Lagomarsino, 1997; Macorini & Izzuddin, 2011), and macroscale models which represent masonry as a homogeneous material. Whereas microscale modelling represents separately units, mortar and adhesion between them, mesoscale modelling lumps the latter two constituents into nonlinear interfaces. Applications of the Discrete Element Method can also be included in this category (Lemos, 2007; Baraldi, et al., 2018). Macroscale descriptions encompass i) generic finite element representations utilising several nonlinear continuum 2D plane stress/3D solid elements (Lourenço, et al., 1997; Berto, et al., 2002; Pelà, et al., 2011; Fu, et al., 2018; Gatta, et al., 2018) for modelling each masonry structural part, and ii) simplified models with macro-elements (Lagomarsino, et al., 2013; Pantò, et al., 2016), where different URM structural components (e.g. pier, spandrel etc.) are represented by specific multi-degree-of-freedom nonlinear elements. In the analysis of entire buildings and monuments, the use of mesoscale approaches with standard computational resources is prohibitive because of the high computational cost. Thus, in practice, numerical simulations for structural assessment are mainly performed employing macroscale models. In general, whichever approach is utilised, realistic predictions can be achieved only when the material model parameters are correctly calibrated. The calibration of mesoscale material parameters is relatively simple, as it is based on non-invasive material tests on small specimens (CUR, 1994). Limitations concerning such type of tests pointed out by many authors (Brencich & de Felice, 2009;

Da Porto, et al., 2010) have been tackled recently by more advanced approaches based on inverse analysis (Sarhosis & Sheng, 2014; Chisari, et al., 2015; Chisari, et al., 2018a). On the other hand, the calibration of macro-model material parameters is problematic, as it should be based upon invasive in-situ tests carried out on large masonry portions (Borri, et al., 2011). Evidently, these tests are expensive and impractical in the case of constructions with historical value, as they may cause substantial damage on large parts of the analysed structure. Thus, macro-models are usually calibrated employing approximate empirical expressions provided by current building codes and based upon previous experience.

A compromise between macro- and micro-modelling is represented by multiscale approaches, which connect material descriptions with different characteristic length scales. They include concurrent methods where the multiple scale models are solved simultaneously and a continuous exchange of information develops between them (Eckardt & Könke, 2008; Reccia, et al., 2018), and homogenisation procedures which assume a clear separation between the scales of representation. Nguyen, et al., (2011) identified three types of homogenisation strategies: analytical homogenisation, computational homogenisation and numerical homogenisation. Methods in the first category (Nemat-Nasser & Hori, 1999) determine analytically an equivalent homogeneous constitutive relationship from the microstructure, and thus they are usually restricted to simple geometries and/or to represent the elastic behaviour. Macro-scale models are usually based on Cauchy continuum, but extensions to micropolar continuum (higher-order homogenisation) have been also proposed to allow for the effects of block rotation (Trovalusci & Masiani, 1996; Trovalusci & Pau, 2014).

Computational homogenisation, as the FE^2 method (Feyel & Chaboche, 2000), is based on online exchange of information between a microscale Representative Volume Element (RVE) and the macroscale domain (Luciano & Sacco, 1997; Massart, et al., 2007; Addessi & Sacco, 2016; Di Re, et al., 2018; Leonetti, et al., 2018). In general, a macroscale model is used for the analysis and its constitutive behaviour is obtained by the solution of a Boundary Value Problem (BVP) for the corresponding RVE. Finally, in numerical homogenisation, the macroscale constitutive model is calibrated offline by fitting the response of a more detailed microscale description (Milani, 2011). Bertolesi et al. (2016) proposed offline homogenisation for masonry components subjected to in-plane loading, in which the mechanical behaviour of a rigid block-nonlinear spring system at the macroscale is defined once and for all at the beginning of the analysis by using a micromodel representing the masonry bond of the cell.

In this paper, a multiscale approach for the calibration of a homogeneous isotropic macroscale model to be used for nonlinear dynamic analysis of masonry structures is proposed. The main objective of the work is to establish a practical and efficient strategy to calibrate macro-models based on the mechanical properties of the constituents. The approach considers energy equivalence between two different scales of representation on the same domain subjected to appropriate boundary conditions. Such equivalence is enforced in a weak sense, where the solution provides the macroscale material properties best fitting the mesoscale response, which acts thus as a virtual test. The approach is then applied to a case study based on previous experimental results on a masonry system subjected to earthquake loading.

2 Multiscale model calibration

2.1 Calibration methodology

The procedure developed in this paper considers a macroscopic representation, here indicated by subscript *M*, and a mesoscopic description, identified by subscript *m* and it assumes a mapping $M: \Omega^m \rightarrow \Omega^M$ between the mesoscale and the macroscale domains. Macroscale and mesoscale models define separately the nonlinear material constitutive laws:

$$\boldsymbol{\sigma}^{\boldsymbol{M}} = f^M\left(\mathcal{H}^M\left(\boldsymbol{x}, \boldsymbol{\kappa}^{\boldsymbol{M}}(\boldsymbol{x})\right), \boldsymbol{\varepsilon}^{\boldsymbol{M}}(\boldsymbol{x})\right) \text{ in } \Omega^M \tag{1a}$$

$$\boldsymbol{\sigma}^{\boldsymbol{m}} = f^m\left(\mathcal{H}^m\left(\boldsymbol{x}, \boldsymbol{\kappa}^{\boldsymbol{m}}(\boldsymbol{x})\right), \boldsymbol{\varepsilon}^{\boldsymbol{m}}(\boldsymbol{x})\right) \text{ in } \Omega^m \tag{1b}$$

where in Eqs (1a,b) the relationship between stress $\boldsymbol{\sigma}$ and strain $\boldsymbol{\varepsilon}$ depends on the position $\boldsymbol{x}$ in the domain Ω through the material model $\mathcal{H}$ at the point and sets of historical variables $\boldsymbol{\kappa}$.

The Hill-Mandel principle of macro-homogeneity (Hill, 1965; Mandel, 1971) is generally used in first-order homogenisation to define the equivalence between the scales in terms of stress power of the RVE:

$$\boldsymbol{\sigma}^{\boldsymbol{M}}:\dot{\boldsymbol{\varepsilon}}^{\boldsymbol{M}}=\frac{1}{V_{RVE}}\int_{V_{RVE}}\boldsymbol{\sigma}^{\boldsymbol{m}}:\dot{\boldsymbol{\varepsilon}}^{\boldsymbol{m}}\,dV \qquad (2)$$

where V_{RVE} is the representative volume. This approach enforces a correspondence between the mechanical response of a single integration point and the average response of the RVE (Figure 1a).

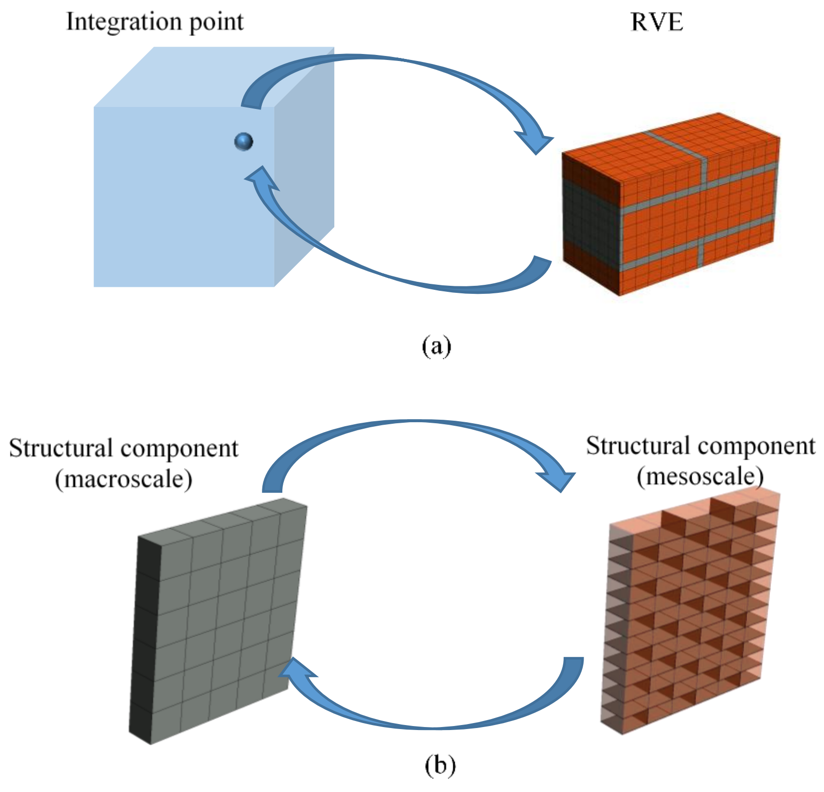

Figure 1. Different approaches for scale transition: (a) first-order homogenisation; (b) proposed multilevel calibration.

In the strain-driven FE^2 approach $\dot{\boldsymbol{\varepsilon}}^{\boldsymbol{M}}$ is evaluated at the integration point from the trial solution of the global problem and applied to the RVE in average as boundary conditions. The Boundary Value Problem is solved for the RVE and the corresponding $\boldsymbol{\sigma}^{\boldsymbol{m}}$ evaluated considering the specific constitutive relationship (1b). Eq. (2) provides $\boldsymbol{\sigma}^{\boldsymbol{M}}$ to be used for the global equilibrium check at the current iteration. Thus, following this approach, the constitutive relationship at macroscale (Eq. (1a)) is defined implicitly. This is the main advantage of this strategy, as it virtually allows for no approximation in the scale transition. However, the approximation of the RVE with a single integration point at the macroscale is acceptable when the stress state at the microscale is uniform, i.e., when the microscale typical length is small compared with the macroscale (principle of separation of scales, Geers et al. 2010). This may not always be the case for masonry structures, and thus some approximations are inevitably introduced. A second very important issue arises when strain localisation occurs at RVE level and the macroscale constitutive relationship presents strain softening, meaning that the macroscopic BVP becomes ill-posed. Regularisation is thus needed (Trovalusci & Masiani, 2003; Massart, et al., 2007; De Bellis & Addessi, 2011; Petracca, et al., 2016; Addessi & Sacco, 2016).

In the procedure proposed here, stress power equivalence between the scales is approximately enforced on the entire domain of the structure, representing a masonry structural component (Figure 1b). The stress power equivalence reads:

$$\int_{\Omega^M} \boldsymbol{\sigma}^{\boldsymbol{M}}: \dot{\boldsymbol{\varepsilon}}^{\boldsymbol{M}} d\Omega^M = \int_{\Omega^m} \boldsymbol{\sigma}^{\boldsymbol{m}}: \dot{\boldsymbol{\varepsilon}}^{\boldsymbol{m}} d\Omega^m + \dot{\epsilon} \tag{3}$$

where now $\dot{\epsilon}$ represents the error rate due to the approximations induced by the specific macromodel utilised.

Considering pseudo-static stress states, the equality between internal and external work implies:

$$\begin{aligned}\int_{\Gamma^M} \boldsymbol{t}^{\boldsymbol{M}} \cdot \dot{\boldsymbol{u}}^{\boldsymbol{M}} d\Gamma^M + \int_{\Omega^M} \boldsymbol{b}^{\boldsymbol{M}} \cdot \dot{\boldsymbol{u}}^{\boldsymbol{M}} d\Omega^M \\ = \int_{\Gamma^m} \boldsymbol{t}^{\boldsymbol{m}} \cdot \dot{\boldsymbol{u}}^{\boldsymbol{m}} d\Gamma^m + \int_{\Omega^m} \boldsymbol{b}^{\boldsymbol{m}} \cdot \dot{\boldsymbol{u}}^{\boldsymbol{m}} d\Omega^m + \dot{\epsilon}\end{aligned} \tag{4}$$

where $\boldsymbol{t}$ are the surface forces on the boundary Γ, while $\boldsymbol{b}$ are volume forces. Neglecting the contribution of these latter for the sake of conciseness and considering the chain rule of differentiation, Eq. (4) finally reads:

$$\int_{\Gamma^M} \left(\boldsymbol{t}^{\boldsymbol{M}} \cdot \dot{\boldsymbol{u}}^{\boldsymbol{M}} - \boldsymbol{t}^{\boldsymbol{m}} \cdot \dot{\boldsymbol{u}}^{\boldsymbol{m}} \frac{\partial \Gamma_i^m}{\partial \Gamma_i^M} \right) d\Gamma_i^M = \dot{\epsilon} \tag{5}$$

Eq. (5) represents the error rate at time *t* due to the scale transition. We can hence define a non-negative monotonically increasing error function:

$$\begin{aligned} \epsilon(t) &= \int_0^t [\dot{\epsilon}(\tau)]^2 d\tau \\ &= \int_0^t \left[\int_{\Gamma^M} \left(\boldsymbol{t}^{\boldsymbol{M}}(\tau) \cdot \dot{\boldsymbol{u}}^{\boldsymbol{M}}(\tau) - \boldsymbol{t}^{\boldsymbol{m}}(\tau) \cdot \dot{\boldsymbol{u}}^{\boldsymbol{m}}(\tau) \frac{\partial \Gamma_i^m}{\partial \Gamma_i^M} \right) d\Gamma_i^M \right]^2 d\tau \end{aligned} \tag{6}$$

The solution of the calibration procedure is given by the solution of the following minimisation problem:

$$\widetilde{\boldsymbol{p}} = \arg\min_{\boldsymbol{p}} \omega_1 \tag{7}$$

where $\omega_1 = \epsilon(T)$ minimises the scale transition error along the whole time *T* of the analysis.

In the case of a single applied displacement *u* at a node, with corresponding force *F*, Eq. (6) becomes:

$$\epsilon(t) = \int_0^t [\dot{\epsilon}(\tau)]^2 d\tau = \int_0^t \left[\left(F^M(\tau) - F^m(\tau) \right) \frac{\partial u(\tau)}{\partial \tau} \right]^2 d\tau \tag{8}$$

and thus:

$$\omega_1 = \int_0^T \left(F^M(t) - F^m(t) \right)^2 \dot{u}^2 \, dt \tag{9}$$

Eq. (9) implies that, in case of monotonic loading at constant velocity, the minimisation of $\epsilon(T)$ reduces to minimisation of the force squared error.

2.2 Features of optimisation problem

In the process described above, it is pointed out that the calibration is performed offline before the actual analysis takes place. It is very important thus to select appropriately the applied loads and their evolution with time, which in the following will be named “pseudo-experimental tests” or “virtual tests”. As general principle, the virtual tests should provide a *robust* identification, meaning that if the calibrated macroscale parameters are applied to a model of the same masonry type under different loading conditions, the results should be sufficiently close to the prediction obtained by means of the mesoscale representation. In the case study in Section 3, it will be seen how the selection of virtual test affects the robustness of the calibration.

Minimising the energy error function (7) can sometimes lead to unrealistic solutions due to intrinsic imperfection of the model to calibrate, and thus some posterior engineering judgement may be required. An example is displayed in Figure 2, where a pseudo-experimental force-displacement curve characterised by very low dissipation is fitted by a trilinear hysteretic elastic-plastic model accounting for stiffness degradation but with linear elastic unloading stiffness, here acting as the macroscale model. Since the model is by nature unable to simulate the stiffness recovering observed at unloading point A, in the search for the best fit of the unloading branch the resulting calibrated model shows a significant stiffness degradation which in turn predicts an unrealistic intersection between the unloading and the elastic loading branches. This is thermodynamically inconsistent in the sense that at the end of a full cycle (from zero force to zero force, point B) the dissipated energy can potentially become negative.

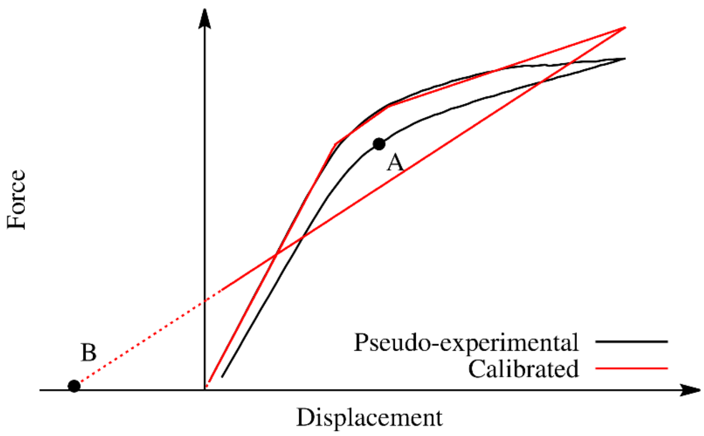

Figure 2. Calibration of an imperfect model: possibility of inconsistent results.

In the case of a single force applied to the system, it is possible to embed this sort of engineering judgement in the optimisation formulation by means of a second error function. From both meso- and macroscale force-displacement plots, similar to that displayed in Figure 2, some suitable engineering features Φ_i, e.g. initial stiffness, yielding force, maximum force, residual displacement at unloading, etc., can be extracted. It is possible to define a second error function related to the features:

$$\omega_2(\boldsymbol{p}) = (\boldsymbol{\Phi}^{\mathbf{M}}(\boldsymbol{p}) - \boldsymbol{\Phi}^{\mathbf{m}})^{\mathbf{T}}\boldsymbol{W}(\boldsymbol{\Phi}^{\mathbf{M}}(\boldsymbol{p}) - \boldsymbol{\Phi}^{\mathbf{m}}) \tag{10}$$

where the features are collected in two vectors $\boldsymbol{\Phi}^{\mathbf{M}}$ and $\boldsymbol{\Phi}^{\mathbf{m}}$, and the quadratic error between meso- and macroscale representation is scaled by a weight matrix $\boldsymbol{W}$ accounting for different physical units. This second error function can act as a regularisation term in the optimisation problem, which now reads:

$$\text{Find } \widetilde{\boldsymbol{p}} \text{ s.t. } \widetilde{\boldsymbol{p}} = \arg\min_{\boldsymbol{p}}[\omega_1(\boldsymbol{p}) + \lambda\, \omega_2(\boldsymbol{p})] \tag{11}$$

In the theoretical case of perfect macromodel, i.e. where there exists a combination of macroscale model parameters which gives an identical response to the mesoscale model, the two objectives ω_1 and ω_2 have a common (zero) minimum, which thus is also the minimum of the regularised function. In general, however, this is not the case and depending on the regularisation parameter λ it is possible to obtain different solutions, and selecting it appropriately may not be easy in most applications.

A more general formulation can be given by transforming the mono-objective optimisation problem (11) into a multi-objective one:

$$\text{Find } \widetilde{\boldsymbol{p}} \text{ s.t. } \widetilde{\boldsymbol{p}} = \arg\min_{\boldsymbol{p}}[\omega_1(\boldsymbol{p}), \omega_2(\boldsymbol{p})] \tag{12}$$

the solution of which is the Pareto Front, i.e. the set of non-dominated solutions (Miettinen, 1999). Several methods exist in general to solve such problem, depending on the type of information available (Marler & Arora, 2004). The dependence of the error functions ω_1, ω_2 on the material parameters $\boldsymbol{p}$ is implicitly defined by the material model $\mathcal{H}^M$ in Eq. (1). The FE analysis acts as a black box function which, after receiving a trial set of material parameters $\boldsymbol{p}$, provides the value of ω. As no information is available about the convexity or even differentiability of this function, a zero-order global optimisation method is advised for solving the problem. In this work, a Genetic Algorithm implemented in the software TOSCA-TS (Chisari & Amadio, 2018) has been utilised. The use of population-based optimisation methods also leads to the solution of problem (12) by tracking the entire Pareto Front, and thus avoiding the need of defining a suitable regularisation parameter λ.

2.3 Mesoscale model

In the mesoscale approach employed in this work (Macorini & Izzuddin, 2011), a masonry element is modelled by explicitly representing units and mortar joints. Mortar and unit–mortar interfaces are lumped into 2D 16-noded zero-thickness nonlinear interface elements. Masonry units are represented by elastic 20-noded solid elements, and possible unit failure in tension and shear is accounted for by means of zero-thickness interface elements placed at the vertical mid-plane of each brick/block (Figure 3). The discretisation for the structure, as proposed in (Macorini & Izzuddin, 2011), consists of two solid elements per unit connected by a unit-unit interface.

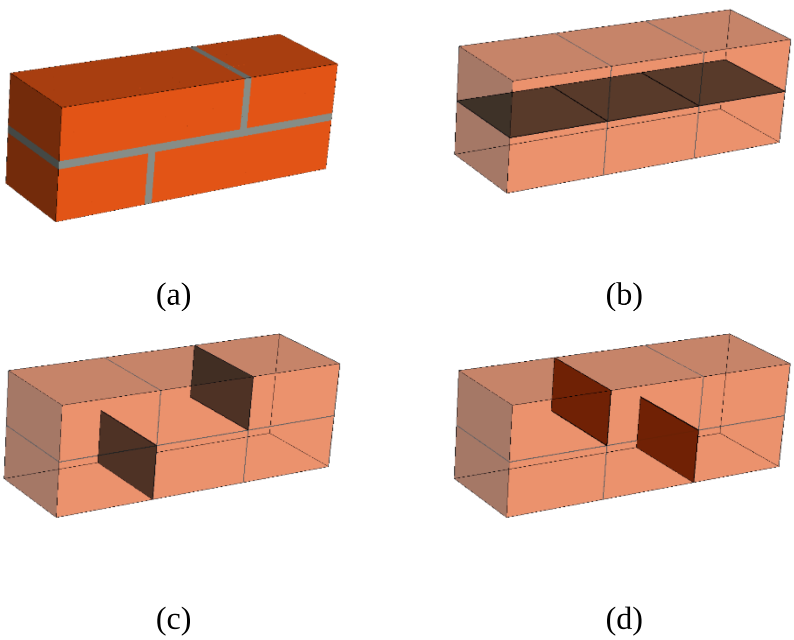

Figure 3. Mesoscale modelling of masonry by means of solid elements for units (in transparency) and zero thickness interfaces: (a) real bond, (b) bed joints, (c) head joints, and (d) brick-brick interfaces.

The interface local material model is formulated in terms of one normal and two tangential tractions $\boldsymbol{\sigma} = \{\tau_x, \tau_y, \sigma\}^T$ and relative displacements $\boldsymbol{u} = \{u_x, u_y, u_z\}^T$ evaluated at each integration point over the reference mid-plane. In the linear range, they are linked one another by uncoupled elastic stiffnesses, which simulate the linear response of the mortar joints, $\boldsymbol{\sigma} = \boldsymbol{k}\, \boldsymbol{u}$.

The material model used for the 16-noded zero-thickness interfaces to simulate the response of both cracks in bricks and mortar joints is based on the coupling of plasticity and damage (Minga, et al., 2018). This approach can simulate all the principal mechanical features of a mortar joint or a dry frictional interface - when mortar is absent - by an efficient formulation that ensures numerical robustness. It can describe i) the softening behaviour in tension and shear, ii) the stiffness degradation depending on the level of damage, iii) the recovering of normal stiffness in compression following crack closure and iv) the permanent (plastic) strains at zero stresses when the interface is damaged.

The yield criterion is represented in the stress space by a conical surface which simulates the behaviour in shear according to the Coulomb law, corresponding to mode II fracture. This surface, defined by cohesion c and friction angle φ, is capped by two planar surfaces representing failure in tension and compression respectively (Figure 4).

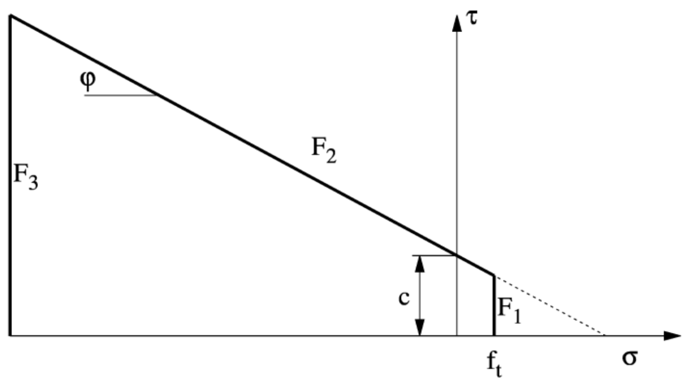

Figure 4. Multi-surface yield criterion (Minga, et al., 2018).

The evolution of the effective stresses is elastic perfectly-plastic, except for the case where the plastic surface F_1, representing failure in tension, is traversed. The damage of the interfaces is defined by a diagonal damage tensor $\boldsymbol{D}$ which controls stiffness degradation and is governed by the plastic work corresponding to each fracture mode. By applying damage to the effective stresses $\bar{\boldsymbol{\sigma}}$, corresponding to the physical stresses developed in the undamaged part of the interface, it is possible to obtain the nominal stresses $\boldsymbol{\sigma}$, defined as:

$$\boldsymbol{\sigma} = (\boldsymbol{I} - \boldsymbol{D})\overline{\boldsymbol{\sigma}} = (\boldsymbol{I} - \boldsymbol{D})\boldsymbol{K}(\boldsymbol{\varepsilon} - \boldsymbol{\varepsilon}^{\boldsymbol{p}}) \tag{13}$$

In this way the implicit solution of the plastic problem and the damage evolution are decoupled, thus allowing for increased efficiency and robustness at the material level. Further details about the material model may be found in (Minga, et al., 2018).

2.4 Macroscale model

The isotropic macroscale model used in this paper is a modified version of the plastic-damage model proposed by Lee & Fenves (1998). In this model a standard decomposition of strains $\boldsymbol{\varepsilon}$ in elastic $\boldsymbol{\varepsilon_e}$ and plastic $\boldsymbol{\varepsilon_p}$ components is considered:

$$\boldsymbol{\varepsilon} = \boldsymbol{\varepsilon}_e + \boldsymbol{\varepsilon_p} \tag{14a}$$

$$\boldsymbol{\varepsilon}_e = \boldsymbol{K}_e^{-1}\boldsymbol{\sigma} \tag{14b}$$

where $\boldsymbol{K_e}$ is the fourth-order isotropic elastic stiffness tensor and $\boldsymbol{\sigma}$ is the nominal Cauchy stress tensor. According to continuum damage mechanics, the nominal stress tensor $\boldsymbol{\sigma}$ is mapped into an effective stress tensor $\overline{\boldsymbol{\sigma}}$:

$$\boldsymbol{\sigma} = (1 - d)\overline{\boldsymbol{\sigma}} \tag{15}$$

where $d = d(\overline{\boldsymbol{\sigma}}, \boldsymbol{\kappa})$ is a scalar global damage variable depending on the stress state and two historical variables $\boldsymbol{\kappa} = (\kappa_t, \kappa_c)^T$ representing the evolution of damage in tension and in compression. The effective stress $\overline{\boldsymbol{\sigma}}$ is defined as the theoretical stress if the stiffness is equal to the initial one $\boldsymbol{K_0}$, and thus:

$$\overline{\boldsymbol{\sigma}} = \boldsymbol{K_0}(\boldsymbol{\varepsilon} - \boldsymbol{\varepsilon_p}) \tag{16}$$

From (14)-(16) the standard plastic-damage constitutive relationship is obtained:

$$\boldsymbol{\sigma} = \boldsymbol{K_e}(\boldsymbol{\varepsilon} - \boldsymbol{\varepsilon_p}) = (1 - d)\boldsymbol{K_0}(\boldsymbol{\varepsilon} - \boldsymbol{\varepsilon_p}) \tag{17}$$

where, following the approach proposed by Lee & Fenves (1998), the evaluation of $\boldsymbol{\varepsilon_p}$ is performed working in the effective stress space. The plastic strain rate is evaluated from the plastic flow potential:

$$\dot{\boldsymbol{\varepsilon}}_{\boldsymbol{p}} = \dot{\lambda} \frac{\partial g}{\partial \overline{\boldsymbol{\sigma}}} \tag{18}$$

with:

$$g(\overline{\boldsymbol{\sigma}}) = \sqrt{(\epsilon f_{t0} \tan \psi)^2 + 3J_2} + \frac{\tan \psi}{3} I_1 \tag{19}$$

where λ plastic multiplier, ϵ flow potential eccentricity, ψ dilation angle, f_{t0} the initial uniaxial tensile stress and I_1, J_2 are the first invariant of stress and the second invariant of deviatoric stress. The incremental plastic problem in the effective stress space reads:

$$\begin{cases} d\overline{\boldsymbol{\sigma}} - \boldsymbol{K_0}\left(d\boldsymbol{\varepsilon} - d\lambda\, \dot{\hat{\boldsymbol{\varepsilon}}}^{\boldsymbol{p}}\right) = \boldsymbol{0} \\ F(\overline{\boldsymbol{\sigma}}, \boldsymbol{\kappa}) = 0 \\ d\boldsymbol{\kappa} - d\lambda \boldsymbol{h}(\overline{\boldsymbol{\sigma}}, \boldsymbol{\kappa}) = \boldsymbol{0} \end{cases} \tag{20}$$

where the yielding function F and the hardening function $\boldsymbol{h}$ are:

$$F(\overline{\boldsymbol{\sigma}}, \boldsymbol{\kappa}) = \frac{1}{1-\alpha} \cdot \left(\alpha I_1 + \sqrt{3J_2} + \beta(\boldsymbol{\kappa})\langle \bar{\sigma}_{max} \rangle - \gamma \langle -\bar{\sigma}_{max} \rangle\right) + \bar{f}_c(\kappa_c) \tag{21a}$$

$$\boldsymbol{h}(\boldsymbol{\sigma}, \boldsymbol{\kappa}) = \begin{pmatrix} r(\boldsymbol{\sigma})\langle \dot{\hat{\varepsilon}}^p_{max} \rangle \\ \left(1 - r(\boldsymbol{\sigma})\right)\langle -\dot{\hat{\varepsilon}}^p_{min} \rangle \end{pmatrix} \tag{21b}$$

with:

- $\beta(\boldsymbol{\kappa}) = -\frac{\bar{f}_c(\kappa_c)}{\bar{f}_t(\kappa_t)}\,(1-\alpha) - (1+\alpha)$;
- $\alpha = \frac{f_{b0r}-1}{2fb0_r-1}$;
- $\gamma = \frac{3(1-K_c)}{2K_c-1}$;
- K_c= Ratio of the second stress invariant on the tensile meridian to that on the compressive meridian at initial yield;
- f_{b0r}= Ratio between biaxial and uniaxial compressive strength;

– $\bar{\sigma}_{max} = \max(\bar{\sigma}_1, \bar{\sigma}_2, \bar{\sigma}_3)$ with $\bar{\sigma}_\mathrm{i}$ principal effective stress;

– $\dot{\varepsilon}^p_{max}$, $\dot{\varepsilon}^p_{min}$= Maximum (resp. minimum) principal components of tensor $\dot{\boldsymbol{\varepsilon}}^{\boldsymbol{p}} = \frac{\partial g}{\partial \bar{\boldsymbol{\sigma}}}$;

– $r(\bar{\boldsymbol{\sigma}}) = \begin{cases} 0 & if\ \bar{\sigma}_1 = \bar{\sigma}_2 = \bar{\sigma}_3 = 0 \\ \frac{\sum_{i=1}^{3}\langle\bar{\sigma}_i\rangle}{\sum_{i=1}^{3}|\bar{\sigma}_i|} & otherwise \end{cases}$;

– $\langle x\rangle = \frac{x+|x|}{2}$.

The scalar damage variable *d* depends on two other scalar variables $d_t(\kappa_t)$ and $d_c(\kappa_c)$, while stiffness recovery is obtained including the dependence on the stress state:

$$d(\bar{\boldsymbol{\sigma}}, \boldsymbol{\kappa}) = 1 - [1 - s_t(\bar{\boldsymbol{\sigma}})\, d_c(\kappa_c)][1 - s_c(\bar{\boldsymbol{\sigma}})\, d_t(\kappa_t)] \tag{22}$$

with:

- $s_t(\bar{\boldsymbol{\sigma}}) = 1 - w_t r(\bar{\boldsymbol{\sigma}})$;
- $s_c(\bar{\boldsymbol{\sigma}}) = 1 - w_c\big(1 - r(\bar{\boldsymbol{\sigma}})\big)$,

where w_t and w_c govern stiffness recovery respectively from compression to tension and viceversa. For the complete definition of the model the four functions $\bar{f}_t(\kappa_t)$, $\bar{f}_c(\kappa_c)$, $d_t(\kappa_t)$ and $d_c(\kappa_c)$ must be defined. In this work, uniaxial strengths in the nominal and in the effective stress space, i.e., functions $f_\chi(\kappa_\chi)$, $\bar{f}_\chi(\kappa_\chi)$, $\chi = t, c$ have been defined and consequently damage variable is obtained as:

$$d_\chi(\kappa_\chi) = 1 - \frac{f_\chi(\kappa_\chi)}{\bar{f}_\chi(\kappa_\chi)} \tag{23}$$

Following Lubliner et al. (1989), both tensile and compressive nominal strengths are expressed as double-exponential function of the relevant historical variable κ_χ, which represents the plastic strain in uniaxial stress states:

$$f_\chi(\kappa_\chi) = f_{\chi 0}\big[(1 + p_{1\chi})e^{-p_{2\chi}\kappa_\chi} - p_{1\chi}e^{-2\,p_{2\chi}\kappa_\chi}\big] \tag{24}$$

where $f_{\chi 0}$ is the initial strength and $p_{1\chi}$, $p_{2\chi}$ parameters to be calibrated (see Appendix). As far as the effective strength is considered, increased robustness is obtained if a hardening behaviour is considered (Minga, et al., 2018) while the introduction of damage allows for modelling both stiffness and strength degradation. The hardening behaviour is expressed as:

$$\bar{f}_\chi(\kappa_\chi) = \begin{cases} f_\chi(\kappa_\chi) & \kappa_\chi < \bar{\kappa}_\chi \\ f_{\chi 0}(p_{4\chi} + p_{3\chi}\kappa_\chi) & \kappa_\chi \geq \bar{\kappa}_\chi \end{cases} \tag{25}$$

where $\bar{\kappa}_\chi = \rho\, \kappa_\chi(f_{\chi,max})$ is the plastic strain at the onset of damage, $\kappa_\chi(f_{\chi,max})$ is the plastic strain at maximum strength and $0 \leq \rho \leq 1$ is a scalar. Eq. (25) implies that the effective plastic strain-stress coincides with $f_\chi(\kappa_\chi)$ while it is linear afterwards (Figure 5). The calibration of parameters $p_{1\chi}$, $p_{2\chi}$, $p_{3\chi}$, $p_{4\chi}$ based on mechanical parameters with physical meaning is described in the Appendix. The material model has been implemented in the FE software ADAPTIC (Izzuddin, 1991).

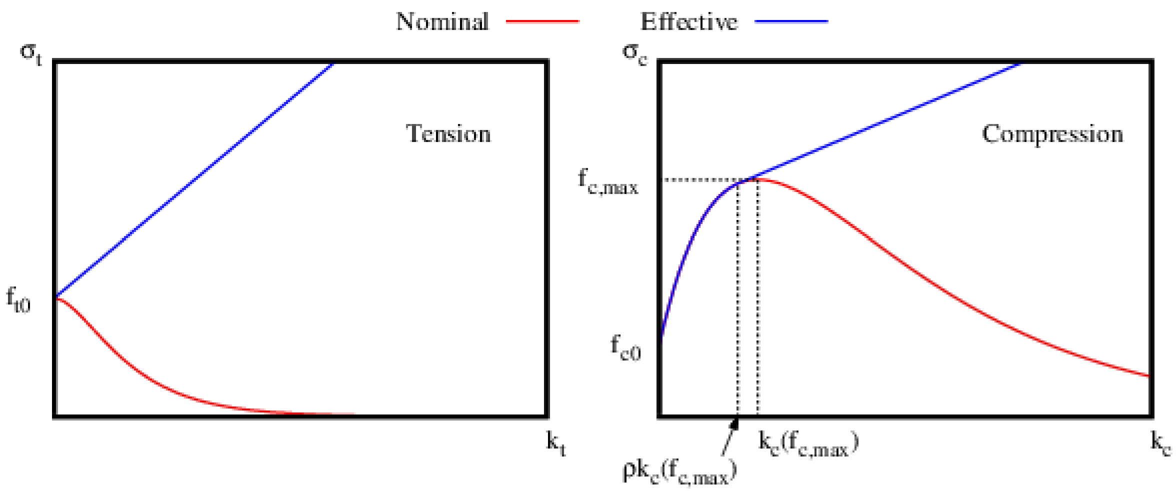

Figure 5. Nominal and effective strength in tension and compression

3 Case study

3.1 Overview

A case study is considered here to illustrate the calibration procedure described in the previous Section. It considers the extensive experimental programme performed within the FP6 European project “ESECMaSE - *Enhanced Safety and Efficient Construction of Masonry Structures in Europe*”.

A two-storey full-scale prototype of a terraced house with rigid base and RC floor slabs was built and tested under pseudo-dynamic loading. The running bond masonry was made of 250mm×175mm×250mm calcium silicate units of type 6DF optimised for the project. The units were assembled with thin mortar bed joints, while the head joints remained unfilled. All these characteristics should lead to a marked orthotropic response, both in the elastic and post-elastic ranges, when the masonry panels are subjected to in-plane loading. Thus, it is of interest to investigate the degree of approximation which is possible to obtain when using an isotropic model, as that described in Section 2.4 which is typically employed for advanced nonlinear analysis of masonry structures, whose material properties are calibrated according to the procedure detailed above.

3.2 Calibration of macroscale material model

Material tests were performed on small wallets to determine basic masonry material properties. Starting from those, the material properties for the mesoscale representation were estimated as reported in

Material	Parameter	Value
Brick	Young's modulus	13620 MPa
	Poisson's ratio	0.253
Concrete	Young modulus	30000 MPa
	Poisson's ratio	0.15
Bed joints	Axial stiffness	34.0 N/mm^3
	Shear stiffness	16.5 N/mm^3
	Tensile strength	0.35 MPa
	Cohesion	0.28 MPa
	Friction angle	atan(0.55)
	Fracture energy (mode I)	0.01 N/mm
	Fracture energy (mode II)	0.2 N/mm
	Fracture energy (compression)	0.5 N/mm
	Damage parameter	0.1
	Compressive strength	23.6 MPa
Brick-brick interface	Axial stiffness	10^4 N/mm^3
	Shear stiffness	10^4 N/mm^3
	Tensile strength	1.49 MPa
	Cohesion	2.235 MPa
	Friction angle	atan(1.0)
	Fracture energy (mode I)	0.1 N/mm
	Fracture energy (mode II)	0.5 N/mm
	Fracture energy (compression)	5 N/mm
	Damage parameter	0.1
	Compressive strength	23.6 MPa

Table 1. More specifically, brick elastic properties and compressive strength were obtained from compressive tests on single units, while brick tensile strength was given by the producer (in general cases it can be estimated by means of indirect tension test). Bed joint stiffness was estimated based on unit and masonry stiffness, considered as spring in series, while bed joint compressive strength represents overall masonry compressive strength in a phenomenological way and was obtained from compressive tests on small wallets. Interface friction coefficient was provided in the ESECMaSE project experimental report and can be estimated from triplet tests along with cohesion. All the other properties were assigned typical values for masonry (CUR, 1994).

Material	Parameter	Value
Brick	Young’s modulus	13620 MPa
	Poisson’s ratio	0.253
Concrete	Young modulus	30000 MPa
	Poisson’s ratio	0.15
Bed joints	Axial stiffness	34.0 N/mm^3
	Shear stiffness	16.5 N/mm^3
	Tensile strength	0.35 MPa
	Cohesion	0.28 MPa
	Friction angle	atan(0.55)
	Fracture energy (mode I)	0.01 N/mm
	Fracture energy (mode II)	0.2 N/mm
	Fracture energy (compression)	0.5 N/mm
	Damage parameter	0.1
	Compressive strength	23.6 MPa
Brick-brick interface	Axial stiffness	10^4 N/mm^3
	Shear stiffness	10^4 N/mm^3
	Tensile strength	1.49 MPa
	Cohesion	2.235 MPa
	Friction angle	atan(1.0)
	Fracture energy (mode I)	0.1 N/mm
	Fracture energy (mode II)	0.5 N/mm
	Fracture energy (compression)	5 N/mm
	Damage parameter	0.1
	Compressive strength	23.6 MPa

Table 1. Material properties of the mesoscale model in the virtual tests.

To calibrate the macroscale model, three virtual tests, involving different failure modes in the masonry, have been considered (Figure 6). In tests (a) and (b) a stiff elastic element is applied on the top of the specimen to transfer the vertical load p=0.5MPa uniformly. Then a horizontal displacement history is imposed at the top. Constraints are applied to the stiff element to couple the vertical displacements and keep the top element horizontal. In the out-of-plane test (c), a uniform stress is applied on one face of the wall, while all edges except the top one are restrained. A load spreader element is utilised to apply a load history on the specimen by controlling the mean displacement of the load application nodes. Load protocol for all tests is characterised by a parabolic curve with maximum displacement equal to 2.5mm for tests (a) and (b) and 1.25mm for tests (c). This protocol has been designed to evaluate the main characteristics of the cyclic response of the specimens, including initial stiffness, peak load, post-peak response and stiffness degradation upon unloading.

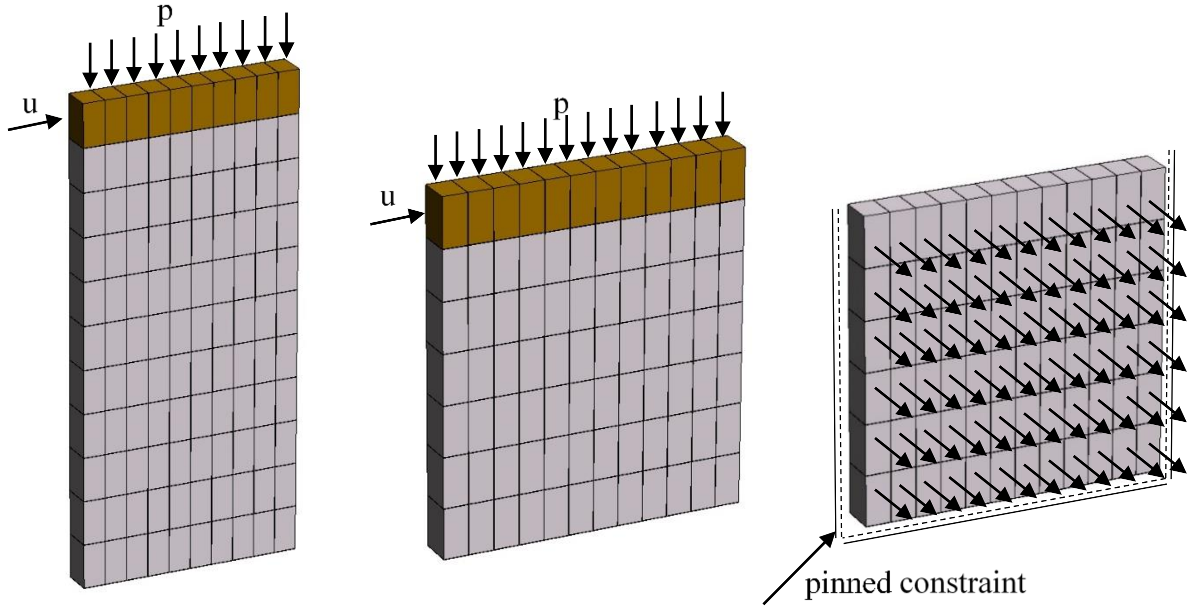

1250mm ×175mm×2500mm (a) | 1500mm×175mm×1500mm (b) | 1500mm×175mm×1500mm (c)

Figure 6. Virtual tests for the calibration of the macromodel.

In Figure 7, the deformed shapes and the force-displacement curves of the three specimens are shown. It is possible to observe the different failure modes predicted for the tests under in-plane loading: (a) flexural failure and (b) shear failure with crack opening at the toes. Diagonal cracks are observed in test (c), with additional flexural crack opening at the base. In terms of force-displacement, the first two tests show quite stable plastic behaviour and reduced dissipation, characteristic of rocking behaviour. On the contrary, the out-of-plane behaviour is characterized by large loss of strength at maximum displacement and significant stiffness degradation at unloading.

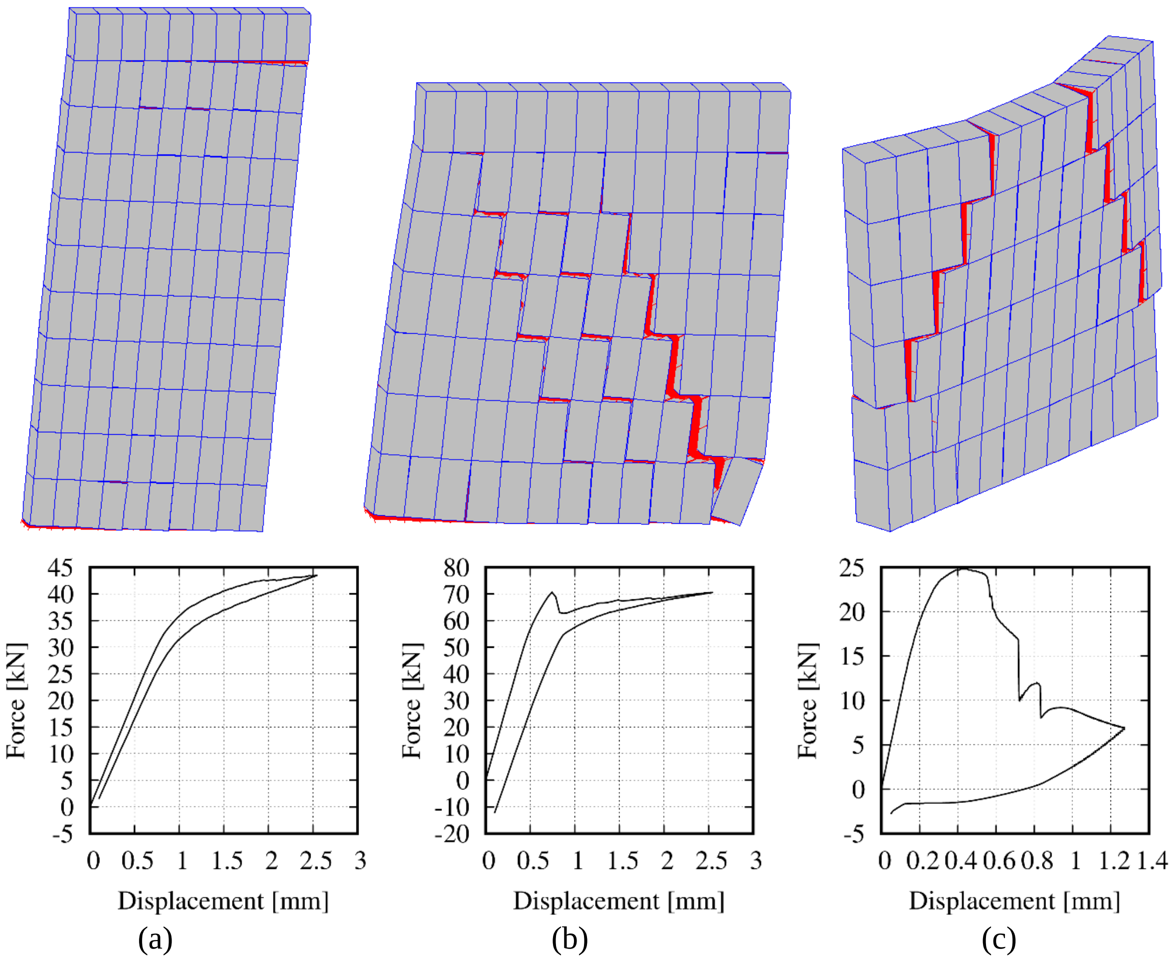

Figure 7. Deformed shapes (magnification factor 50) at maximum displacement and force-displacement plots for the virtual tests.

The virtual tests were then modelled by the macroscale approach. Twenty-noded solid elements with average dimensions equal to 250mm×250mm ×175mm were used, and the material model described in Section 2.4 was considered to represent the nonlinear behaviour of masonry at the macroscale. The model material parameters and their ranges of variation are displayed in

Parameter	**Definition**	**Minimum**	**Maximum**

E	Young’s modulus	100 MPa	5000 MPa
ν	Poisson’s ratio	0.001	0.499
$\tilde{f}_{bo}$	Ratio between biaxial and uniaxial compressive strength	0.9	1.5
ψ	Dilation angle	0°	90°
ϵ	Flow potential eccentricity	0.05	0.15
w_t	Tension stiffness recovery factor	0.0	1.0
w_c	Compression stiffness recovery factor	0.0	1.0
f_{t0}	Initial uniaxial tensile strength	0.01 MPa	1.0 MPa
G_t	Fracture energy in uniaxial tension	1e-5 N/mm	0.1 N/mm
μ	Parameter controlling stiffness degradation in tension	0.0	1.0
$f_{c,max}$	Maximum uniaxial compressive strength	5.0 MPa	30.0 MPa
$\tilde{f}_y$	Ratio between uniaxial yielding stress and maximum strength in compression	0.01	1.0
$k_{c,fmax}$	Plastic strain in compression at $f_{c,max}$	1e-5	1e-2
ρ_c	Ratio of $k_{c,fmax}$ where damage in compression starts	0.0	1.0

Table 2.

Parameter	**Definition**	**Minimum**	**Maximum**
E	Young’s modulus	100 MPa	5000 MPa
ν	Poisson’s ratio	0.001	0.499
$\tilde{f}_{bo}$	Ratio between biaxial and uniaxial compressive strength	0.9	1.5
ψ	Dilation angle	0°	90°
ϵ	Flow potential eccentricity	0.05	0.15
w_t	Tension stiffness recovery factor	0.0	1.0
w_c	Compression stiffness recovery factor	0.0	1.0
f_{t0}	Initial uniaxial tensile strength	0.01 MPa	1.0 MPa
G_t	Fracture energy in uniaxial tension	1e-5 N/mm	0.1 N/mm
μ	Parameter controlling stiffness degradation in tension	0.0	1.0
$f_{c,max}$	Maximum uniaxial compressive strength	5.0 MPa	30.0 MPa
$\tilde{f}_y$	Ratio between uniaxial yielding stress and maximum strength in compression	0.01	1.0
$k_{c,fmax}$	Plastic strain in compression at $f_{c,max}$	1e-5	1e-2
ρ_c	Ratio of $k_{c,fmax}$ where damage in compression starts	0.0	1.0

Table 2. Material parameters for the macromodel.

The optimization problem (12) for each virtual test was solved by means of a Non-dominated Sorting Genetic Algorithm (NSGA-II, Deb et al. 2002) implemented in TOSCA-TS (Chisari & Amadio, 2018) using the parameters specified in Table 3.

Parameter	Value
Population	50 individuals
Initial population generation	Sobol algorithm (Sobol, 1967)
Number of generations	50
Selection	Stochastic Universal Sampling, with linear ranking based on domination and scaling pressure equal to 2.0 (Baker, 1987)
Crossover	Blend-α, with α=2.0 (Eshelman & Schaffer, 1992)
Crossover probability	1.0
Mutation probability	0.007

Table 3: GA parameters adopted for the calibration.

In the application of definition (5) in tests (a,b) the contribution of the vertical load was neglected for the sake of simplicity. Following the discussion about regularisation of the calibration problem in Section 2.2, a second objective related to the horizontal force-displacement curve was added to the optimisation problem. It reads:

$$\omega_2(\boldsymbol{p}) = (\boldsymbol{\Phi}^{\mathbf{M}}(\boldsymbol{p}) - \boldsymbol{\Phi}^{\mathbf{m}})^{\mathbf{T}}\boldsymbol{W}(\boldsymbol{\Phi}^{\mathbf{M}}(\boldsymbol{p}) - \boldsymbol{\Phi}^{\mathbf{m}}) \tag{26}$$

where:

- $\boldsymbol{\Phi} = [K_{in} \quad K_{fin} \quad F_y \quad F_{max} \quad F(u_{max}) \quad F_{fin}]^T$;
- K_{in}, K_{fin} respectively initial and final stiffness;
- F_y, F_{max}, $F(u_{max})$, F_{fin} respectively yielding force, maximum force, force at maximum displacement, force at final displacement;
- $\boldsymbol{W} = diag\left(\left[\left(F^m_{max}/K^m_{in}\right)^2 \quad \left(F^m_{max}/K^m_{in}\right)^2 \quad 1 \quad 1 \quad 1 \quad 1 \quad 1\right]\right)$.

Considering the three tests individually as calibration tests, three Pareto Fronts were obtained and then considered as solutions of the multi-objective optimisation problem.

The results shown in Figure 8 allow to draw some conclusions on the calibration procedure and on the macromodel employed. On the main diagonal of the matrix, the force-displacement plots of the solutions are compared to the pseudo-experimental results obtained in the relevant virtual test used in the calibration. It is possible to see that in all cases a good agreement is obtained, meaning that: (i) there exists at least one set of material parameters fitting with satisfactory accuracy any of the three tests used in the procedure, and (ii) the optimisation procedure is able to find such solution. Conclusion (i) however does not guarantee that such three sets are coincident, that is, there exists a unique set of parameters fitting with satisfactory accuracy all three virtual tests at the same time. It is important thus to study how the solutions predict the response in tests not used in the calibration (Chisari, et al., 2018b). This is shown in the off-diagonal plots in Figure 8.

In case of a calibration performed by means of test (a) or (c), the calibrated parameters applied to the other tests show both large variability and low accuracy (first and third rows in Figure 8). In particular, maximum load and global stiffness are largely overestimated in both tests (b) and (c) with the solutions from test (a), while with the solutions from test (c) stiffness degradation is overestimated in tests (a) and (b), and initial stiffness is underestimated. The curves in the second row in Figure 8, however, show that a calibration performed with test (b) can predict reasonably well the behaviour of the specimen under test (a), while, again, relatively large variability of the prediction is observed for test (c). In any case, it is possible to find some solutions fitting with sufficient accuracy the response of the out-of-plane virtual test.

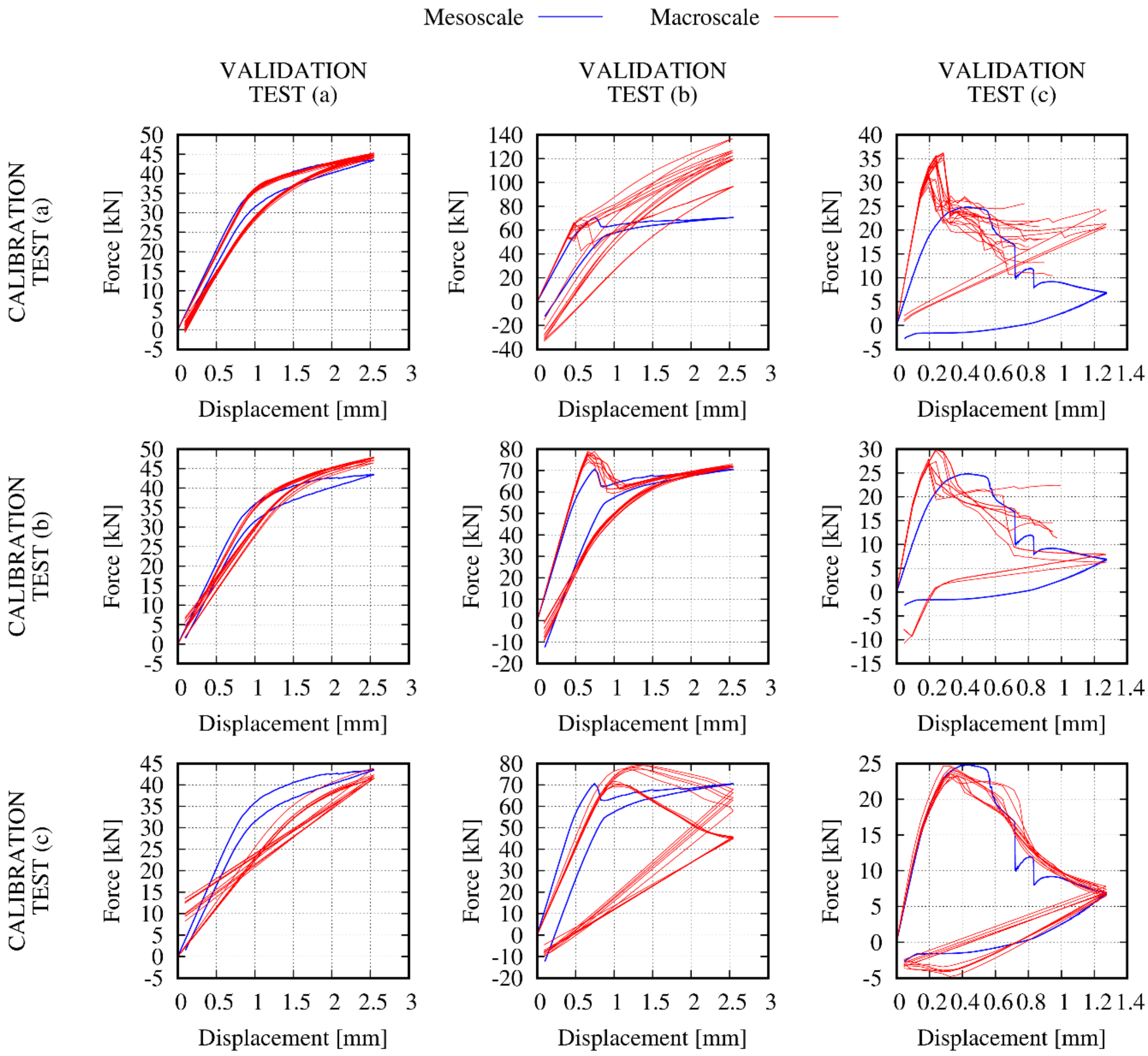

Figure 8. Results of the calibration and validation.

Among all the solutions obtained by calibration with test (b), the one with minimum discrepancy from the mesoscale test (c) results was then assumed as final solution. This is characterised by the values reported in

Parameter	Value
E	2850 MPa
ν	0.31
$\tilde{f}_{bo}$	1.23
ψ	16°
ϵ	0.13
w_t	0.87
w_c	0.16
f_{t0}	0.215 MPa
G_t	9.11e-3 N/mm
μ	0.216
$f_{c,max}$	18.4
$\tilde{f}_y$	1.0
$k_{c,fmax}$	7e-4
ρ_c	0.299

Table 4.

Parameter	Value
E	2850 MPa
ν	0.31
$\tilde{f}_{bo}$	1.23
ψ	16°
ϵ	0.13
w_t	0.87
w_c	0.16
f_{t0}	0.215 MPa
G_t	9.11e-3 N/mm
μ	0.216
$f_{c,max}$	18.4
$\tilde{f}_y$	1.0
$k_{c,fmax}$	7e-4
ρ_c	0.299

Table 4. Final solution of the macroscale calibration.

The deformed shape and tensile damage pattern, which is a crack indicator in the continuum, are displayed in Figure 9. Comparing these results with Figure 7, it is possible to appreciate that a correctly calibrated model seems to be able to capture the main damage patterns as observed in the mesoscale representation in all cases.

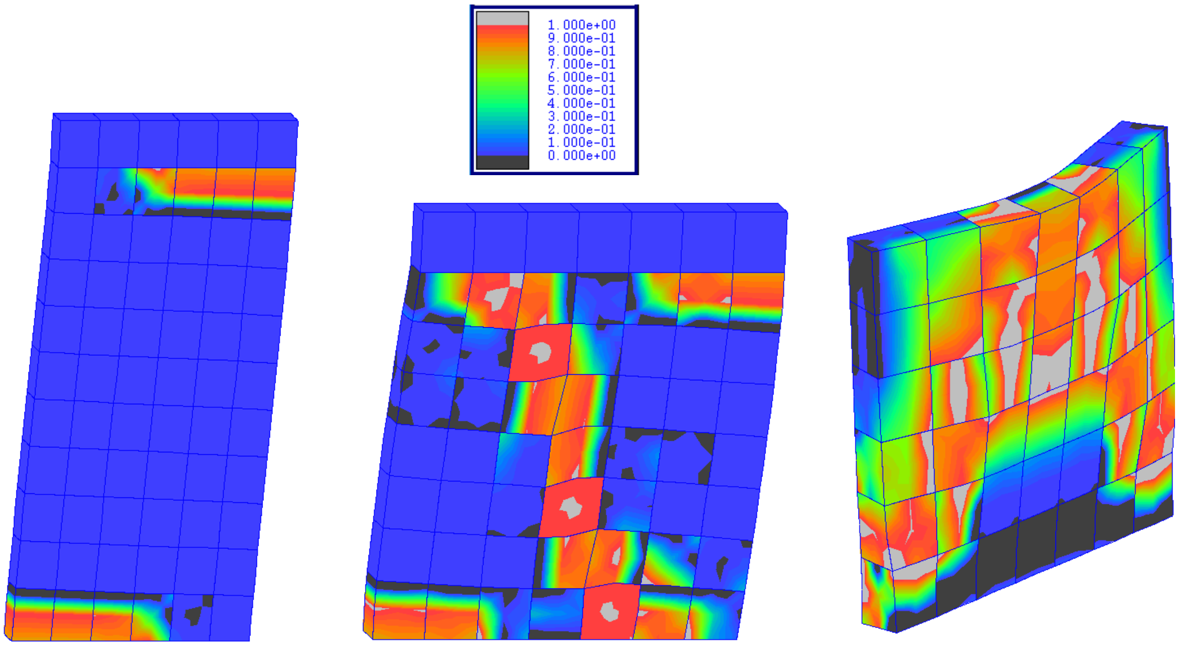

(a) (b) (c)

Figure 9. Deformed shapes (same amplification as in Figure 7) and tensile damage patterns for the calibrated macromodels.

3.3 Validation against pseudo-dynamic test

The calibrated macromodel was then used to predict the response of the two-storey structure subjected to pseudo-dynamic loading. The specimen (Figure 10a) representing half of a symmetric two-storey terraced house with rigid base was tested at the ELSA Reaction-wall Laboratory of the JRC (Anthoine & Capéran, 2008). It was characterised by floor plan dimensions of 5.30m×4.75m and a 5.40m height. The pseudo-dynamic test simulated the application of an earthquake along the short wall direction (x direction in Figure 10b).

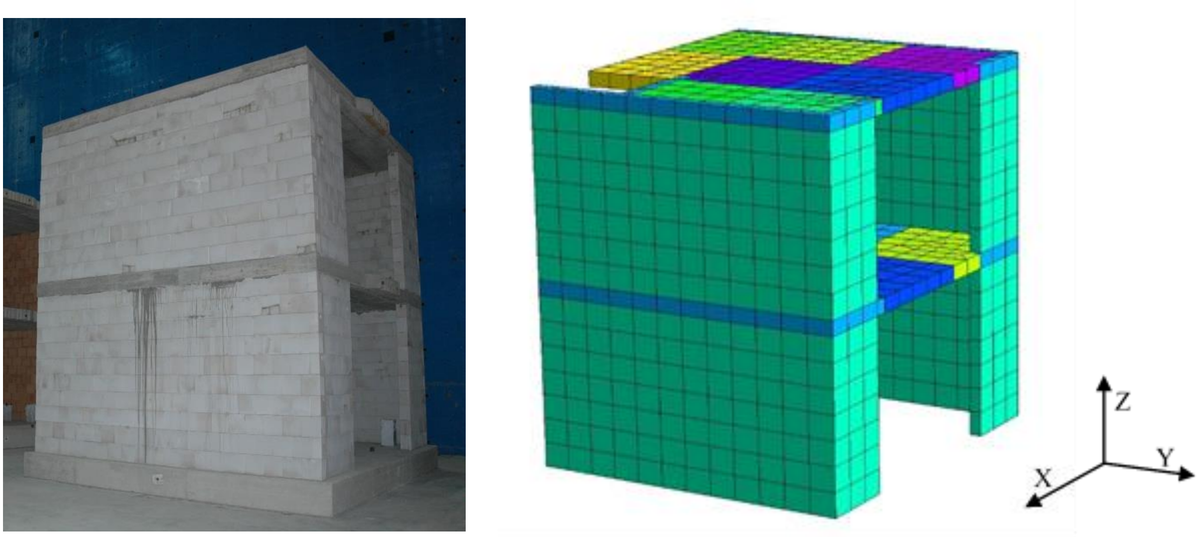

(a) (b)

Figure 10. Pseudo-dynamic test: (a) view of the structure (courtesy of Dr Armelle Anthoine), and (b) numerical model. The different colours in (b) represents different applied loads.

A 3D solid numerical model of the building was developed (Figure 10b), where the walls were modelled with the nonlinear model described in Section 2.4 and calibrated in Section 3.2. The concrete floor was represented by means of elastic elements with Young's modulus equal to 30GPa, typical of the concrete type utilised. The additional masses on the first and second floor were equal to the experimental added masses reproducing design dead and live loads (4.52t on the first floor and 7.39t on the second floor). Such masses were distributed on the floor plane in the real test such as to minimise the eccentricity between centre of mass and centre of stiffness in y direction (orthogonal to the ground motion) and thus to have a mainly translational motion of the structure along x.

In the pseudo-dynamic test, the equations of motion for a simplified 2-dof mechanical system were solved iteratively online using experimentally observed stiffness to obtain the corresponding relative displacements to apply to the structure by means of actuators at floor level. The ground motion considered was a 10.23s long artificially generated time history matching the EUROCODE 8 (EN 1998-1-1, 2005) design spectrum with elastic response spectrum type I, peak ground acceleration PGA=0.04g and soil type B. It was then scaled to PGA=0.12g corresponding to the acceleration for which the first significant damage was experimentally observed. Two numerical modelling approaches concerning the loading history are considered here:

a) Dynamic analysis with application of the ground motion at the base;
b) Dynamic (pseudo-static) analysis with experimental displacements applied at the floors.

In case (b), the experimental floor displacements have been previously fitted with a spline. By differentiating the spline twice, it was possible to obtain an approximate acceleration history to apply at floor level. This was deemed convenient to run a dynamic analysis which is generally more stable than a displacement-controlled static analysis since inertial terms make the problem better conditioned even in case of loss of stiffness. The results of the numerical analyses in terms of force-displacement plots are displayed in Figure 11.

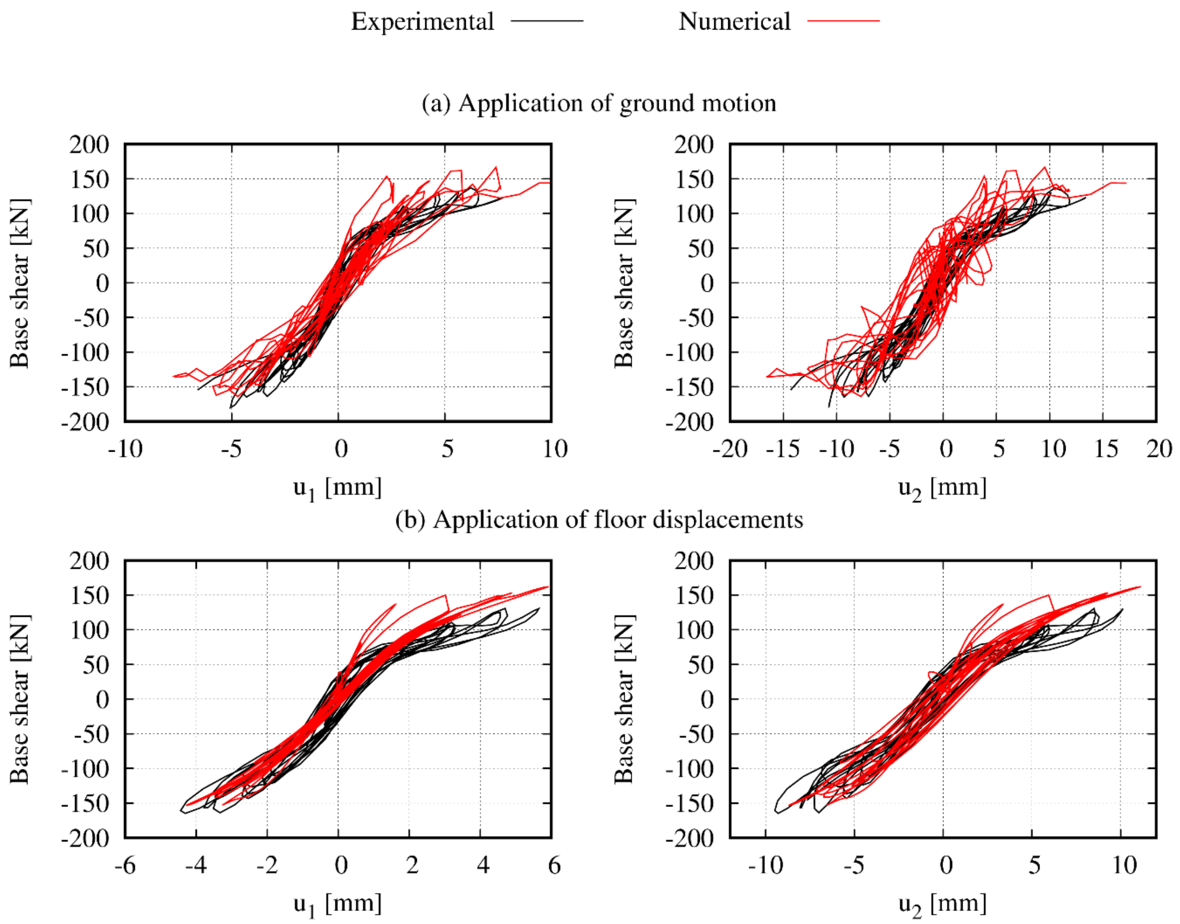

Figure 11. Base shear-floor displacement plots for experimental tests and numerical models.

They are displayed until the numerical model reached convergence, which is equal to 6.3s for model (a) (applied base acceleration history) and 5.66s for model (b) (applied displacements at the floors). After that the structure completely lost its stiffness and no meaningful results could be obtained. Looking at Figure 11, it is possible to notice a very good agreement between the experimental data and the numerical output in terms of force-displacement curves as far as stiffness, maximum force and maximum displacement is concerned. In model (b) larger strength is predicted by the numerical model in the first steps of the load history, but this is reasonable as the numerical model is initially undamaged while the experimental specimen had undergone previous tests with lower accelerations which could have provoked damage and strength degradation. Furthermore, in Figure 12 it is evident that the spline approximation induces larger displacements at the beginning of the analysis, and consequently larger forces. The comparison between base shear force after t=3s shows a very good agreement between experimental results and numerical predictions.

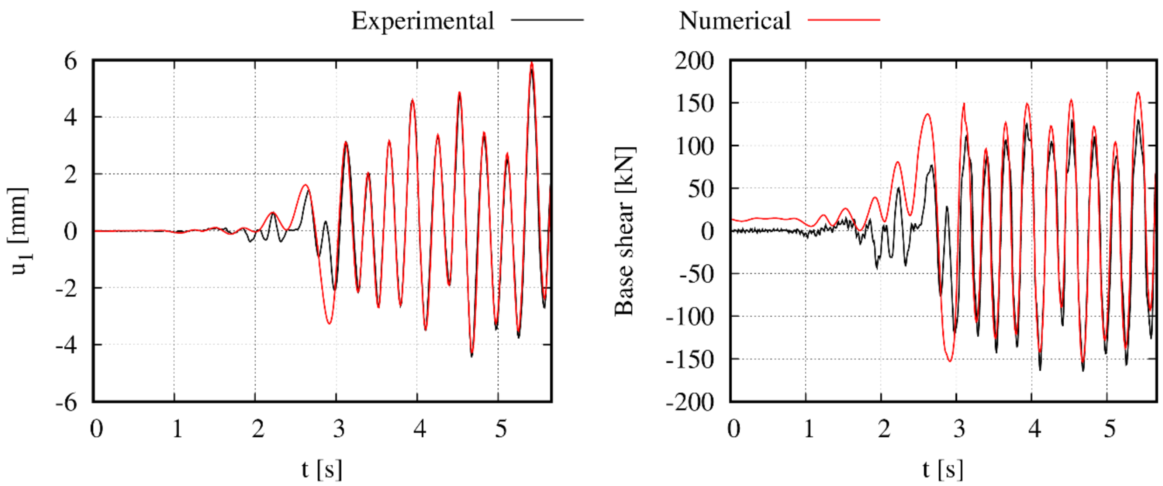

Figure 12. Comparison between applied displacements at first floor and resulting forces for model (b).

The contour of damage variable d_t can be assumed as an approximation of cracking occurrence in a homogenous model. It is shown in Figure 13 for models (a) and (b) at time t=5.5s, when damage has generally occurred.

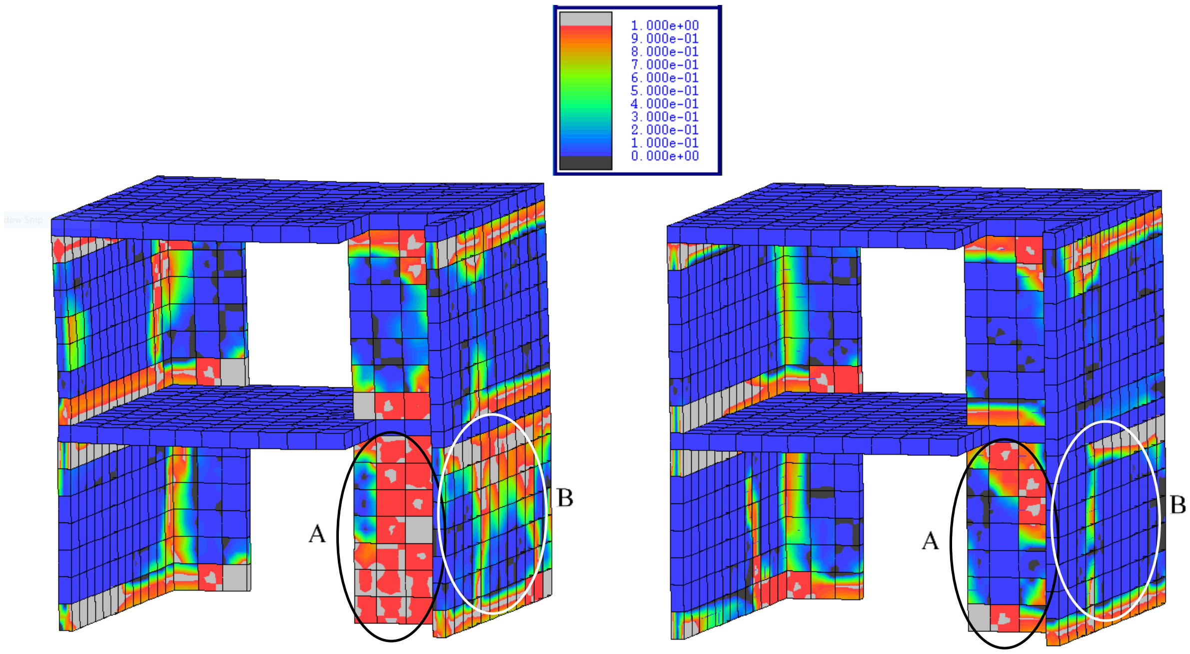

(a) (b)

Figure 13. Damage contour at t=5.5s: (a) model with applied ground motion, and (b) model with applied floor displacements.

The comparison between the damage contours in models (a,b) shows that they are generally different and rather more spread in model (a), where, unlike model (b) a shear wall results almost completely damaged (A marker in Figure 13). Even in the long wall orthogonal to this damage is more accentuated (B marker). It is believed that in case of model (a) the additional mass distribution was not perfectly able to cancel floor rotations leading thus to a more severe stress state on the structure. In Figure 14 model (b), which more closely reproduces the test loading protocol as effectively performed, is compared to the experimental cracking pattern.

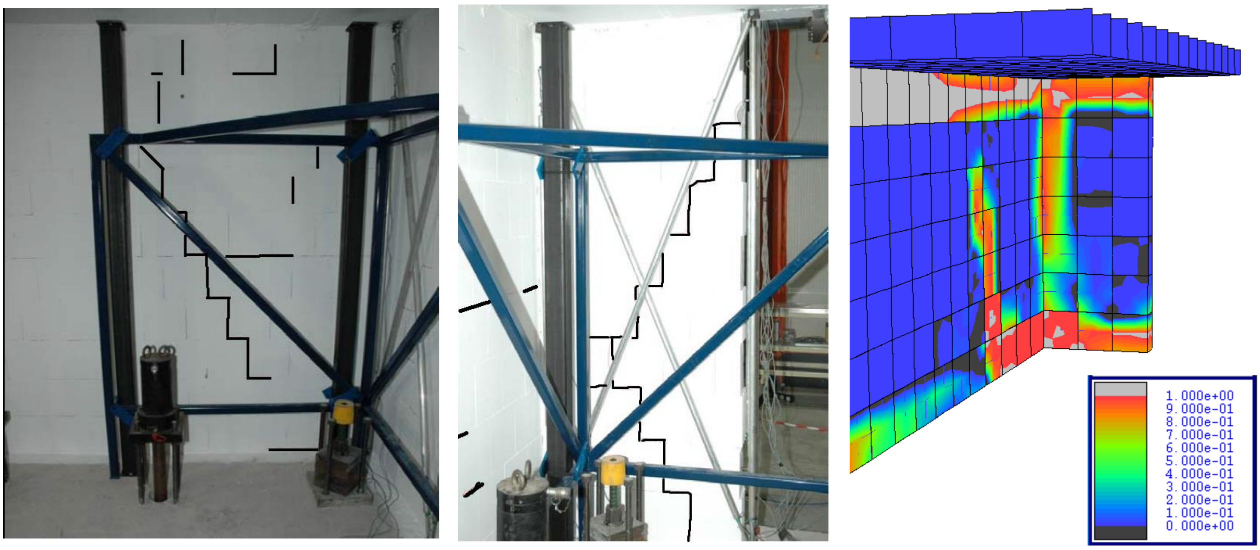

(a) (b) (c)

Figure 14. Comparison between experimental cracking pattern (courtesy of Dr Armelle Anthoine) and numerical damage contour for model (b): cracking patterns (a) in the long wall, (b) in the short wall, and (c) damage contour at the intersection between the two walls.

It is possible to see that the damage can generally represent the cracking in the wall, even though, especially in the short wall, a shift toward the intersection between floors and wall and between orthogonal walls is visible in the numerical model. It is believed that the limitations of using an isotropic model for such an anisotropic material, as the masonry utilised for the test, greatly justify such discrepancy. A similar shift was observed in the comparison of the other wider wall on the opposite side of the building (Figure 15).

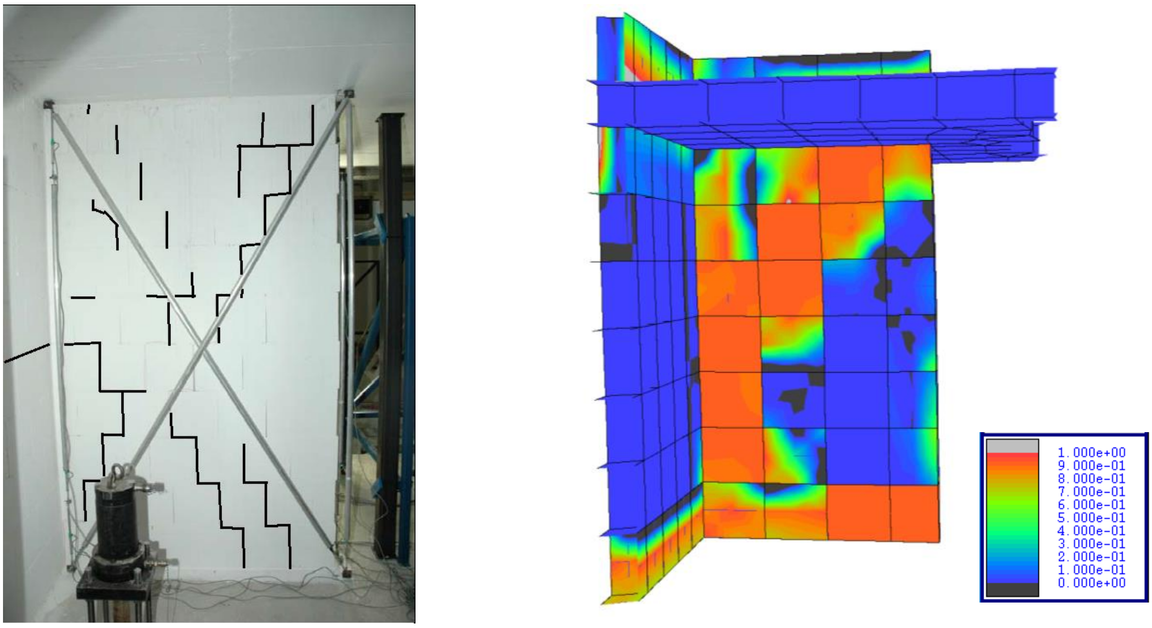

(a) (b)

Figure 15. Comparison between (a) experimental cracking pattern (courtesy of Dr Armelle Anthoine) and (b) numerical damage pattern for model (b): wider wall in the direction of the motion.

4 Conclusion

In this paper, a multiscale model calibration procedure is proposed to provide an efficient and accurate framework for the use of approximate macroscale models in the prediction of the response of masonry structures under extreme loading, including earthquakes. The methodology utilises two different scales of representation for the same structural component. The mesoscale representation, which can be calibrated by means of material tests on constituents, is taken as virtual test for the calibration of the more approximate and computationally efficient macroscale model. The latter calibration is performed by means of minimisation of energy discrepancy. A case study is presented involving experimental tests performed on a running bond masonry with large blocks and unfilled head joints. The results highlight the importance of careful selection of the virtual test, which needs to be able to represent different failure modes of masonry material. In the cases studied, calibration performed by means of a shear test on a square panel leading to diagonal and flexural failure allows for a robust prediction of the response under different in-plane loading conditions. However, as far as the out-of-plane response is concerned the accuracy of the prediction can deteriorate despite achieving a good fit with the calibration response. This implies that information regarding out-of-plane behaviour needs to be included in the calibration process, suggesting that a mixed in-plane/out-of-plane virtual test could lead to a calibrated model with superior predictive capability. The selection of the optimal virtual tests, which clearly depends on the model to calibrate, will be considered in further developments.

The validation of the calibrated models has been performed considering an entire building subjected to earthquake loading. The numerical prediction has shown remarkable agreement with the experimental response in terms of force-displacement curves. An improved approximation of the crack pattern by means of damage contours in the macroscale model could be potentially achieved by employing an enhanced orthotropic material model, which is currently under study.

Acknowledgements

This research has been supported by the European Commission through the Marie Skłodowska-Curie Individual Fellowship "MultiCAMS – *Multi-level Model Calibration for the Assessment of Historical Masonry Structures*", Project no. 744400. The data related to the experimental tests performed within the ESECMaSE project were kindly provided by Dr Armelle Anthoine. The support of the Research Computing Service at Imperial College is also gratefully acknowledged.

Appendix

Parameter $p_{1\chi}$ can be evaluated based on the ratio between initial and maximum strength. In fact, the maximum of function (24) is:

$$f_{\chi,max} = \frac{f_{\chi 0}\left(1 + p_{1\chi}\right)^2}{4p_{1\chi}} \tag{A.1}$$

from which:

$$p_{1\chi} = 2\frac{f_{\chi,max}}{f_{\chi 0}} - 1 + 2\sqrt{\left(\frac{f_{\chi,max}}{f_{\chi 0}}\right)^2 - \frac{f_{\chi,max}}{f_{\chi 0}}} \tag{A.2}$$

In tension there is no hardening, so $f_{t0} = f_{t,max}$ and $p_{1t} = 1$.

The value of $p_{2\chi}$ can be evaluated starting from either (1) the value of plastic strain at maximum strength $\kappa_\chi\left(f_{\chi,max}\right)$, or (2) fracture energy. In case (1), used for the curve in compression, the condition of maximum strength is obtained imposing:

$$\frac{df_\chi}{d\kappa_\chi} = 0 = f_{\chi 0}\left[-p_{2\chi}\left(1 + p_{1\chi}\right)e^{-p_{2\chi}\kappa_\chi} + 2p_{1\chi}p_{2\chi}e^{-2\,p_{2\chi}\kappa_\chi}\right] \tag{A.3}$$

from which:

$$p_{2\chi} = \frac{1}{\kappa_\chi\left(f_{\chi,max}\right)}\log\frac{2p_{1\chi}}{1 + p_{1\chi}} \tag{A.4}$$

In case (2), utilised for the curve in tension, fracture energy density g_χ is defined as the area under the $f_\chi\left(\varepsilon_\chi\right)$ curve from the onset of cracking:

$$g_\chi = \frac{G_\chi}{l} = \int_{f_{\chi 0}/E}^{+\infty} f_\chi d\varepsilon_\chi \tag{A.5}$$

Since

$$\varepsilon_\chi = \varepsilon_\chi^{el} + \kappa_\chi = \frac{\bar{f}_\chi}{E} + \kappa_\chi \tag{A.6}$$

it follows that:

$$d\varepsilon_\chi = \frac{\partial\varepsilon_\chi}{\partial\kappa_\chi}d\kappa_\chi = \left(\frac{1}{E}\frac{\partial\bar{f}_\chi}{\partial\kappa_\chi} + 1\right)d\kappa_\chi = \left(\frac{p_{3\chi}f_{\chi 0}}{E} + 1\right)d\kappa_\chi \tag{A.7}$$

and so Eq. (A.5) becomes:

$$\begin{aligned} g_\chi &= \int_{f_{\chi 0}/E}^{+\infty} f_\chi d\varepsilon_\chi = \left(\frac{p_{3\chi}f_{\chi 0}}{E} + 1\right)\int_0^{+\infty} f_\chi d\kappa_\chi \\ &= \left(\frac{p_{3\chi}f_{\chi 0}}{E} + 1\right)\frac{f_{\chi 0}}{p_{2\chi}}\left(1 + \frac{p_{1\chi}}{2}\right) \end{aligned} \tag{A.8}$$

$p_{3\chi}$ can be evaluated differently in tension or in compression. In the first case, a fairly intuitive definition (see also Minga et al. 2018) can be given providing the ratio $\mu = \kappa_{s\chi}/\varepsilon_s$ between residual plastic strain $\kappa_{s\chi}$ and total strain ε_s at unloading when the plastic work in monotonic loading has reached $s \cdot g'_\chi$ where $g'_\chi = \int_0^{+\infty} f_\chi d\kappa_\chi$. The plastic work reads:

$$\begin{aligned} W_p &= \int_0^{\kappa_\chi} f_\chi(\tau) d\tau \\ &= \frac{f_{\chi 0}}{2 p_{2\chi}} e^{-2 p_{2\chi} \kappa_\chi} \left(e^{p_{2\chi}\kappa_\chi} - 1\right)\left[p_{1\chi}\left(e^{p_{2\chi}\kappa_\chi} - 1\right) + 2\, e^{p_{2\chi}\kappa_\chi}\right] \\ &= \frac{g'_\chi}{\left(2 + p_{1\chi}\right)} \left(1 - e^{-p_{2\chi}\kappa_\chi}\right)\left[p_{1\chi}\left(1 - e^{-p_{2\chi}\kappa_\chi}\right) + 2\right] = s\, g'_\chi \end{aligned} \tag{A.9}$$

Defining $\tilde{\kappa}_\chi = 1 - e^{-p_{2\chi}\kappa_\chi}$, Eq. (A.7) becomes:

$$p_{1\chi}\tilde{\kappa}_\chi^2 + 2\tilde{\kappa}_\chi - s\left(2 + p_{1\chi}\right) = 0 \tag{A.10}$$

whose meaningful solution is:

$$\tilde{\kappa}_\chi = 1 - e^{-p_{2\chi}\kappa_\chi} = \frac{-1 + \sqrt{1 + s\, p_{1\chi}\left(2 + p_{1\chi}\right)}}{p_{1\chi}} \tag{A.11}$$

and thus the corresponding κ_χ is:

$$\kappa_{s\chi} = -\frac{\log\left(1 - \tilde{\kappa}_\chi\right)}{p_{2\chi}} \tag{A.12}$$

Imposing $\kappa_{s\chi} = \mu\, \varepsilon_s$ it follows that:

$$p_{3\chi} = \frac{1 - \mu}{\mu} \frac{E}{f_{\chi 0}} - \frac{1}{\kappa_{s\chi}} \tag{A.13}$$

Substituting (A.13) in (A.8), the final expression for $p_{2\chi}$ can be obtained:

$$p_{2\chi} = \frac{1}{\mu}\left(\frac{g'_\chi}{f_{\chi 0}\left(1 + \frac{p_{1\chi}}{2}\right)} - \frac{f_{\chi 0}}{E \log\left(1 - \tilde{\kappa}_\chi\right)}\right)^{-1} \tag{A.14}$$

In compression $p_{3\chi}$ is evaluated imposing the continuity of tangent at $\bar{\kappa}_\chi = \rho\, \kappa_\chi\left(f_{\chi,max}\right)$:

$$p_{3\chi} = \frac{1}{f_{\chi 0}} \frac{\partial f_\chi}{\partial \kappa_\chi}\bigg|_{\bar{\kappa}_\chi} = -p_{2\chi}(1 + p_{1\chi})e^{-p_{2\chi}\bar{\kappa}_\chi} + 2p_{1\chi}p_{2\chi}e^{-2\,p_{2\chi}\bar{\kappa}_\chi} \tag{A.15}$$

Finally, $p_{4\chi}$ is evaluated imposing the value of strength at $\bar{\kappa}_\chi$:

$$p_{4\chi} = f_\chi(\bar{\kappa}_\chi)/f_{\chi 0} - p_{3\chi}\bar{\kappa}_\chi \tag{A.16}$$

References

Addessi, D. & Sacco, E., 2016. Enriched plane state formulation for nonlinear homogenization of in-plane masonry wall. *Meccanica*, 51(11), pp. 2891-2907.

Anthoine, A. & Capéran, P., 2008. *Earthquake tests and analysis of the experimental results,* European Laboratory for Structural Assessment (ELSA), Ispra (Italy): Deliverable 8.3 ESECMaSE project.

Baker, J. E., 1987. *Reducing bias and inefficiency in the selection algorithm.* Hillsdale, New Jersey, s.n., pp. 14-21.

Baraldi, D., Reccia, E. & Cecchi, A., 2018. In plane loaded masonry walls: DEM and FEM/DEM models. A critical review. *Meccanica,* 53(7), pp. 1613-1628.

Bertolesi, E., Milani, G. & Lourenço, P. B., 2016. Implementation and validation of a total displacement non-linear homogenization approach for in-plane loaded masonry. *Computers and Structures,* Volume 176, pp. 13-33.

Berto, L., Saetta, A., Scotta, R. & Vitaliani, R., 2002. An orthotropic damage model for masonry structures. *International Journal for Numerical Methods in Engineering,* Volume 55, pp. 127-157.

Borri, A., Castori, G., Corradi, M. & Speranzini, E., 2011. Shear behavior of unreinforced and reinforced masonry panels subjected to in situ diagonal compression tests. *Construction and Building Materials,* 25(12), pp. 4403-4414.

Brencich, A. & de Felice, G., 2009. Brickwork under eccentric compression: Experimental results and macroscopic models. *Construction and Building Materials,* 23(5), pp. 1935-1946.

Chisari, C. & Amadio, C., 2018. TOSCA: a Tool for Optimisation in Structural and Civil engineering Analyses. *International Journal of Advanced Structural Engineering,* 10(4), pp. 401-419.

Chisari, C., Macorini, L., Amadio, C. & Izzuddin, B., 2018a. Identification of mesoscale model parameters for brick-masonry. *International Journal of Solids and Structures,* Volume 146, pp. 224-240.

Chisari, C., Macorini, L., Amadio, C. & Izzuddin, B. A., 2015. An Inverse Analysis Procedure for Material Parameter Identification of Mortar Joints in Unreinforced Masonry. *Computers and Structures,* Volume 155, pp. 97-105.

Chisari, C., Rizzano, G., Amadio, C. & Galdi, V., 2018b. Sensitivity analysis and calibration of phenomenological models for seismic analyses. *Soil Dynamics and Earthquake Engineering,* Volume 109, pp. 10-22.

CUR, 1994. *Structural masonry: a experimental/numerical basis for practical design rules,* Gouda, The Netherlands: CUR.

Da Porto, F., Guidi, G., Garbin, E. & Modena, C., 2010. In-plane behavior of clay masonry walls: Experimental testing and finite-element modeling. *Journal of Structural Engineering,* 136(11), pp. 1379-1392.

De Bellis, M.L. & Addessi, D., 2011. A cosserat based multi-scale model for masonry structures. *International Journal for Multiscale Computational Engineering,* 9(5), pp. 543-563.

Deb, K., Pratap, A., Agarwal, S. & Meyarivan, T., 2002. A Fast and Elitist Multiobjective Genetic Algorithm: NSGA-II. *IEEE Transactions on Evolutionary Computation,* 6(2), pp. 182-197.

Di Re, P., Addessi, D. & Sacco, E., 2018. A multiscale force-based curved beam element for masonry arches. *Computers and Structures,* Volume 208, pp. 17-31.

Eckardt, S. & Könke, C., 2008. Adaptive damage simulation of concrete using heterogeneous multiscale models. *Journal of Algorithms & Computational Technology,* Volume 2, p. 275–297.

EN 1998-1-1, 2005. *Eurocode 8: Design of structures for earthquake resistance-Part 1: General rules, seismic actions and rules for buildings.*. s.l.:European Standard.

Eshelman, L. J. & Schaffer, J. D., 1992. Real-coded Genetic Algorithms and interval schemata. In: *Foundations of Genetic Algorithms.* San Mateo: Morgan-Kaufman, pp. 187-202.

Feyel, F. & Chaboche, J., 2000. FE2 multiscale approach for modelling the elastoviscoplastic behaviour of long fibre SiC-Ti composite materials. *Computer Methods in Applied Mechanics and Engineering,* Volume 183, pp. 309-330.

Fu, Q., Qian, J. & Beskos, D. E., 2018. Inelastic anisotropic constitutive models based on evolutionary linear transformations on stress tensors with application to masonry. *Acta Mechanica,* 229(2), pp. 719-743.

Gambarotta, L. & Lagomarsino, S., 1997. Damage models for the seismic response of brick masonry shear walls. Part I: the mortar joint model and its applications. *Earthquake Engineering and Structural Dynamics,* 26(4), pp. 423-439.

Gatta, C., Addessi, D. & Vestroni, F., 2018. Static and dynamic nonlinear response of masonry walls. *International Journal of Solids and Structures,* Volume 155, pp. 291-303.

Geers, M. G. D., Kouznetsova, V. G. & Brekelmans, W. A. M., 2010. Multi-scale computational homogenization: Trends and challenges. *J. Comput. Appl. Math.,* Volume 234, pp. 2175-2182.

Hill, R., 1965. A self-consistent mechanics of composite materials. *Journal of the Mechanics and Physics of Solids,* 13(4), pp. 213-222.

Izzuddin, B. A., 1991. *Nonlinear dynamic analysis of framed structures.* Imperial College London: PhD Thesis.

Lagomarsino, S., Penna, A., Galasco, A. & Cattari, S., 2013. TREMURI program: An equivalent frame model for the nonlinear seismic analysis of masonry buildings. *Engineering Structures,* Volume 56, pp. 1787-1799.

Lee, J. & Fenves, G., 1998. Plastic-damage model for cyclic loading of concrete structures. *Journal of Engineering Mechanics,* 124(8), pp. 892-900.

Lemos, J., 2007. Discrete element modeling of masonry structures. *International Journal of Architectural Heritage,* 1(2), pp. 190-213.

Leonetti, L. et al., 2018. A multiscale damage analysis of periodic composites using a couple-stress/Cauchy multidomain model: Application to masonry structures. *Composites Part B: Engineering,* Volume 141, pp. 50-59.

Lotfi, H. R. & Shing, P., 1994. Interface model applied to fracture of masonry structures. *Journal of structural engineering,* 120(1), pp. 63-80.

Lourenço, P. B., de Borst, R. & Rots, J. G., 1997. A plane stress softening plasticity model for orthotropic materials. *International Journal for Numerical Methods in Engineering,* Volume 40, pp. 4033-4057.

Lourenço, P. B. & Rots, J. G., 1997. Multisurface Interface Model for Analysis of Masonry Structures. *Journal of Engineering Mechanics*, 123(7), pp. 660-668.

Lubliner, J., Olver, J., Oller, S. & Oñate, E., 1989. A plastic-damage model for concrete. *International Journal of Solids and Structures,* 25(3), pp. 299-326.

Luciano, R. & Sacco, E., 1997. Homogenization technique and damage model for old masonry material. *International Journal of Solids and Structures,* 34(24), pp. 3191-3208.

Macorini, L. & Izzuddin, B., 2011. A non-linear interface element for 3D mesoscale analysis of brick-masonry structures. *International Journal of Numerical Methods in Engineering,* Volume 85, pp. 1584-1608.

Mandel, J., 1971. *Plasticité classique et viscoplasticité.* Vienna-New York: Springer-Verlag.

Marler, R. & Arora, J., 2004. Survey of multi-objective optimization methods for engineering. *Structural and Multidisciplinary Optimization*, 26(6), pp. 369-395.

Massart, T., Peerlings, R. & Geers, M., 2007. An enhanced multi-scale approach for masonry wall computations with localization of damage. *International Journal for Numerical Methods in Engineering,* Volume 69, pp. 1022-1059.

Miettinen, K., 1999. *Nonlinear multiobjective optimization.* s.l.:Springer.

Milani, G., 2011. Simple homogenization model for the non-linear analysis of in-plane loaded masonry walls. *Computers and Structures*, 89(17-18), pp. 1586-1601.

Minga, E., Macorini, L. & Izzuddin, B., 2018. A 3D mesoscale damage-plasticity approach for masonry structures under cyclic loading. *Meccanica*, 53(7), pp. 1591-1611.

Nemat-Nasser, S. & Hori, M., 1999. *Micromechanics: Overall Properties of Heterogeneous Materials.* 2nd ed. Amsterdam: Elsevier.

Nguyen, V., Stroeven, M. & Sluys, L., 2011. Multiscale continuous and discontinuous modeling of heterogeneous materials: A review on recent developments. *Journal of Multiscale Modelling,* 3(4), pp. 229-270.

Pantò, B., Cannizzaro, F., Caddemi, S. & Caliò, I., 2016. 3D macro-element modelling approach for seismic assessment of historical masonry churches. *Advances in Engineering Software,* Volume 97, pp. 40-59.

Pelà, L., Cervera, M. & Roca, P., 2011. Continuum damage model for orthotropic materials: Application to masonry. *Computer Methods in Applied Mechanics and Engineering,* Volume 200, pp. 917-930.

Petracca, M. et al., 2016. Regularization of first order computational homogenization for multiscale analysis of masonry structures. *Computational Mechanics,* 57(2), pp. 257-276.

Reccia, E., Leonetti, L., Trovalusci, P. & Cecchi, A., 2018. A multiscale/multidomain model for the failure analysis of masonry walls: a validation with a combined fem/dem approach. *International Journal for Multiscale Computational Engineering*, 16(4), pp. 325-343.

Sarhosis, V. & Sheng, Y., 2014. Identification of material parameters for low bond strength masonry. *Engineering Structures*, Volume 60, pp. 100-110.

Sobol, I., 1967. Distribution of points in a cube and approximate evaluation of integrals. *U.S.S.R Comput. Maths. Math. Phys,* Volume 7, pp. 86-112.

Trovalusci, P. & Masiani, R., 1996. Cosserat and Cauchy materials as continuum models of brick masonry. *Meccanica,* Volume 31, pp. 421-432.

Trovalusci, P. & Masiani, R., 2003. Non-linear micropolar and classical continua for anisotropic discontinuous materials. *International Journal of Solids and Structures*, 40(5), pp. 1281-1297.

Trovalusci, P. & Pau, A., 2014. Derivation of microstructured continua from lattice systems via principle of virtual works: the case of masonry-like materials as micropolar, second gradient and classical continua. *Acta Mechanica,* 225(1), pp. 157-177.